



Theory of the jets ejected after the inertial collapse of cavities with applications to bubble bursting jets

José M. Gordillo * and Francisco J. Blanco-Rodríguez 

*Área de Mecánica de Fluidos, Departamento de Ingeniería Aeroespacial y Mecánica de Fluidos,
Universidad de Sevilla, 41092 Sevilla, Spain*



(Received 27 February 2023; accepted 13 July 2023; published 26 July 2023)

The dynamics of the axisymmetric jets originated from the bursting of bubbles in a liquid of density ρ , viscosity μ , and interfacial tension coefficient σ can be rationalized as a two-stage process in which, initially, the pressure jump $\sim \sigma/R_b$ accelerates the liquid towards the axis of symmetry, inducing a far-field flow rate per unit length $Q_\infty \propto V_c R_b$, with R_b and $V_c = \sqrt{\sigma/(\rho R_b)}$ indicating the radius of the bubble and the capillary velocity, respectively. The second stage, during which a fast jet of radius $R_{\text{jet}}(T) \ll R_b$ and velocity $V_{\text{jet}}(T) \gg V_c$ is ejected, is driven by the far-field radial velocity field established initially, which forces the collapse of the cavity walls while keeping Q_∞ practically constant in time because liquid inertia and mass conservation prevent appreciable changes of this quantity during the very short timescale characterizing the ejection of the jet. Our theoretical predictions for $R_{\text{jet}}(T)$ and $V_{\text{jet}}(T)$ reproduce fairly well the time evolution of the jet width and of the jet velocity for over three decades in time, obtaining good agreement with numerical simulations from the instant of jet inception until $R_{\text{jet}} \sim R_b$. The analytical expressions for the jet width and for the jet velocity provided here constitute the initial conditions for the explicit solution of the ballistic equations deduced in Gekle and Gordillo [*J. Fluid Mech.* **663**, 293 (2010)], which, hence, can be straightforwardly used in order to quantify the size and velocity of the first drop ejected and the fluxes of mass, momentum, and energy transferred from the ocean into the atmosphere. In addition, motivated by the results obtained for the particular case of bubble bursting jets, we also present here a unified theoretical framework aimed at quantifying the dynamics of the type of generic jets produced by the collapse of axisymmetric gas cavities of arbitrary shape when their implosion is forced by the radial velocity induced by a far-field boundary condition expressing that the dimensionless liquid flow rate per unit length directed towards the axis of symmetry, q_∞ , remains constant in time. Making use of theory and of full numerical simulations, we first analyze the case of the collapse of a conical bubble with a half-opening angle β finding that, when the value of q_∞ is fixed to a constant, this type of axisymmetric jets converge towards a purely inertial β -dependent self-similar solution of the inviscid Navier-Stokes equations, described here for the first time, which is characterized by the fact that the jet width and velocity are respectively given, in the limit $\beta \ll 1$, by $r_{\text{jet}} \approx 2.25 \tan \beta \sqrt{q_\infty \tau}$ and $v_{\text{jet}} \approx 3q_\infty / (2 \tan \beta \sqrt{q_\infty \tau})$, with τ indicating the dimensionless time after the jet is ejected. For the case of parabolic cavities with a dimensionless radius of curvature at the plane of symmetry r_c , our theory predicts that $r_{\text{jet}} \propto (2r_c)^{-1/2} (q_\infty \tau)^{3/4}$ and $v_{\text{jet}} \propto q_\infty (2r_c)^{1/2} (q_\infty \tau)^{-3/4}$, a result which is also in good

*jgordill@us.es

agreement with full numerical simulations. The present results might also find applications in the description of the very fast jets, with velocities reaching up to 1000 m s^{-1} , produced after a bubble cavitates very close to a wall and in the quantification of the so-called bazooka effect.

DOI: [10.1103/PhysRevFluids.8.073606](https://doi.org/10.1103/PhysRevFluids.8.073606)

I. INTRODUCTION

It is known that the type of high speed liquid jets produced after the implosion of a bubble, widely used in applications related with the cleaning of surfaces [1], is partly responsible for the structural damage in cavitating flows [2] and plays a key role in the dispersion of contaminants [3,4]. These high speed jets, which share similarities with those formed by the so-called bazooka effect [5] also possess applications in medicine, where they could be used in needle-free drug injection systems [6,7] and are commonly observed after the impact of either a drop [8–13] or a solid [14,15] against a gas-liquid interface and after the collapse of bubbles [16–19]. To our knowledge, and in spite of the number of recent contributions on the subject, there does not exist a commonly accepted framework capable of predicting the dynamics of the myriad of types of fast and thin inertial liquid jets produced after the implosion of a cavity. Hence, it will be our main purpose here to present a theory to describe the dynamics of the jets ejected after the collapse of slender axisymmetric cavities whose predictions will be compared with the results of full numerical simulations carried out using GERRIS [20,21].

The velocities of the jets produced after the implosion of a cavity depend very much on the initial geometry of the interface from which they are ejected, which justifies classifying the jets in, at least, two different categories: (i) the jets produced at the axis of an initially spherical surface and (ii) the jets produced at the base of a truncated conical surface. For instance, the type of jets reported Refs. [7,22], which can be analyzed as a function of the initial near-axis nonuniform radial velocity field at the interface [23] and are employed, for instance, in ink-jet printing applications [24,25], belong to the type of jets emerging from the bottom of a spherical cap. The jets produced by the cavitation of bubbles near boundaries [26,27] also belong to the same type of jets when the so-called standoff parameter, which expresses the ratio between the initial distance of the bubble center to the boundary and the maximum bubble radius, is of order unity or larger. Indeed, when the value of the standoff parameter is $\lesssim O(0.1)$, Ref. [2] presented numerical results retaining compressibility effects in the simulations revealing that the jets produced by cavitation bubbles near a rigid boundary do not emerge from an initially smooth, locally spherical cap, but from the base of a truncated conical interface. This numerical result was later confirmed experimentally in Ref. [28], in which velocities of the order of $\sim 100 \text{ m/s}$ for the case of jets produced by cavitation bubbles emanating from a spherical cap were measured, i.e., for values of the standoff parameter of order unity, and much larger velocities, of the order of $\sim 1000 \text{ m/s}$, for the case of jets emerging from the base of a truncated conical bubble, a result in agreement with the original finding reported in Ref. [2]. Moreover, Ref. [28] realized that the jets emanating from the base of the locally conical bubble are the result of a boundary-parallel cylindrical flow converging towards the axis of symmetry and, motivated by this fact, Reuter and Ohl [28] also reported the results of simplified numerical simulations neglecting compressibility effects, obtaining results in agreement with their own experimental measurements.

It will be the main purpose in this contribution to describe both numerically and theoretically the “conical jets,” namely the jets emerging from the base of a truncated conical interface. The conical jets, which are comparatively faster than those emerging from a spherical cap, are found not only in the collapse of cavitation bubbles for small values of the standoff parameter but also in other types of natural flows, like in the bursting of bubbles at an interface [12,29–31] or after the impact of a drop on a liquid pool [9–12]. Indeed, in these two latter cases, before the jet is ejected, capillary

waves traveling along the interface towards the bottom of the cavity deform the initially spherical bubble into a truncated cone [32]. Moreover, our analysis on the collapse of conical cavities is also extended here to the case of cavities with a generic shape, paying special attention to parabolic cavities, because this is the type of void geometry found when a solid impacts a free surface [14,15].

The paper is structured as follows: Section II is devoted to present the results of numerical simulations of bubble bursting jets, which motivates the theory in Sec. III, where we analyze the ejection of jets from slender axisymmetric cavities whose collapse is forced by a constant value of the flow rate per unit length. In this section, we also compare the predictions of our theory with the results of the numerical simulations presented in Sec. II and with the numerical results in Appendix A, where we also deduce a new self-similar axisymmetric solution of the inviscid Navier-Stokes equations that, up to our knowledge, had not been reported before. Conclusions are presented in Sec. IV.

II. BUBBLE BURSTING JETS: NUMERICAL RESULTS

Due to their widespread presence in nature and in technological applications, an increasing number of numerical [14,29,30,33], experimental [10,11,13,19,34], and theoretical [35,36] studies have been devoted to characterize the width and speed of the jets ejected after the collapse of a cavity or a bubble, a process which is ubiquitously present in our daily life experience. A type of jets exhaustively studied in recent times because of their crucial role played in the generation of nanometric sea spray aerosol are the jets produced after the bursting of bubbles see, e.g., Refs. [4,31,37–45], which break into a number of droplets that inject mass, heat, and momentum into the surrounding atmosphere, hence, influencing climate [33,46,47]. The only result in the literature suggesting a prediction for the time evolution of the width $R_{\text{jet}}(T)$ and velocity $V_{\text{jet}}(T)$ of bubble bursting jets; see Fig. 1, which is the necessary intermediate step to properly quantify the different fluxes transported by these jets, is the study of Lai, Eggers, and Deike [36], where the authors suggested that the inertio-capillary self-similar solution first reported in Ref. [35] governs the dynamics of bubble bursting jets. Therefore, the solution proposed in Ref. [36] is characterized by the fact that inertial terms in the momentum equation for a liquid of density ρ , viscosity μ , and interfacial tension coefficient σ are supposed to be in balance with the capillary pressure terms, a fact implying that $\rho V_{\text{jet}}^2(T) \propto \sigma/R_{\text{jet}}(T)$ and, consequently, $We_l = \rho V_{\text{jet}}^2(T) R_{\text{jet}}(T)/\sigma$ should remain constant in time [35]: In this contribution, we show that this is not the case and deduce, for the first time, the correct equations for $R_{\text{jet}}(T)$ and $V_{\text{jet}}(T)$.

In order to first test whether We_l remains constant in time, we have performed simulations of the type depicted in Fig. 1 using GERRIS [20,21] because this numerical code has been proven to accurately reproduce experimental results related with the bursting of bubbles [30,31]. In the following, the bubble radius R_b and the capillary velocity $V_c = \sqrt{\sigma/(\rho R_b)}$ are used to build dimensionless variables, written in lowercase to differentiate them from their dimensional counterparts, written in capitals, i.e., $r_{\text{jet}}(\tau) = R_{\text{jet}}(\tau)/R_b$, $v_{\text{jet}}(\tau) = V_{\text{jet}}(\tau)/V_c$, and $We_l(\tau) = v_{\text{jet}}^2 r_{\text{jet}}$ with $t = TV_c/R_b$ and $\tau = t - t_{\text{bubble}}$ referring to the dimensionless time after the jet is ejected; see Figs. 1 and 2. Here we consider that the Bond number verifies the condition $Bo = \rho g R_b^2/\sigma \ll 1$, with g indicating gravity and, therefore, the jet ejection process is controlled, for fixed values of the density and viscosity ratios see Fig. 1, by just one dimensionless parameter, namely the Ohnesorge number, defined as $Oh = \mu/\sqrt{\rho R_b \sigma}$, related with the Laplace number as $La = Oh^{-2}$, a parameter which is varied here within the range $625 \leq La \leq 17\,000$, with each value of La identified using the color code of Fig. 2(a).

The jets depicted in Fig. 1 are emitted once the capillary wave with a dimensionless wavelength $\lambda^* \propto Oh^{1/2}$, propagating with the Oh-independent dimensionless speed ≈ 5 , reaches the bottom of the cavity at the instant $t_{\text{bubble}}(La)$ depicted in Fig. 2(a) [32]. The capillary wave deforms the initial spherical bubble into a truncated conical surface with a half-opening angle $\beta(La)$ such that $\beta \simeq 45^\circ$ for $La \geq 2500$; see the green dashed line in the third panel of Fig. 1, as well as Figs. 3 and Fig. 1 in the Supplemental Material [48]. For $La \geq 2500$, the minimum radius of the truncated cone is given

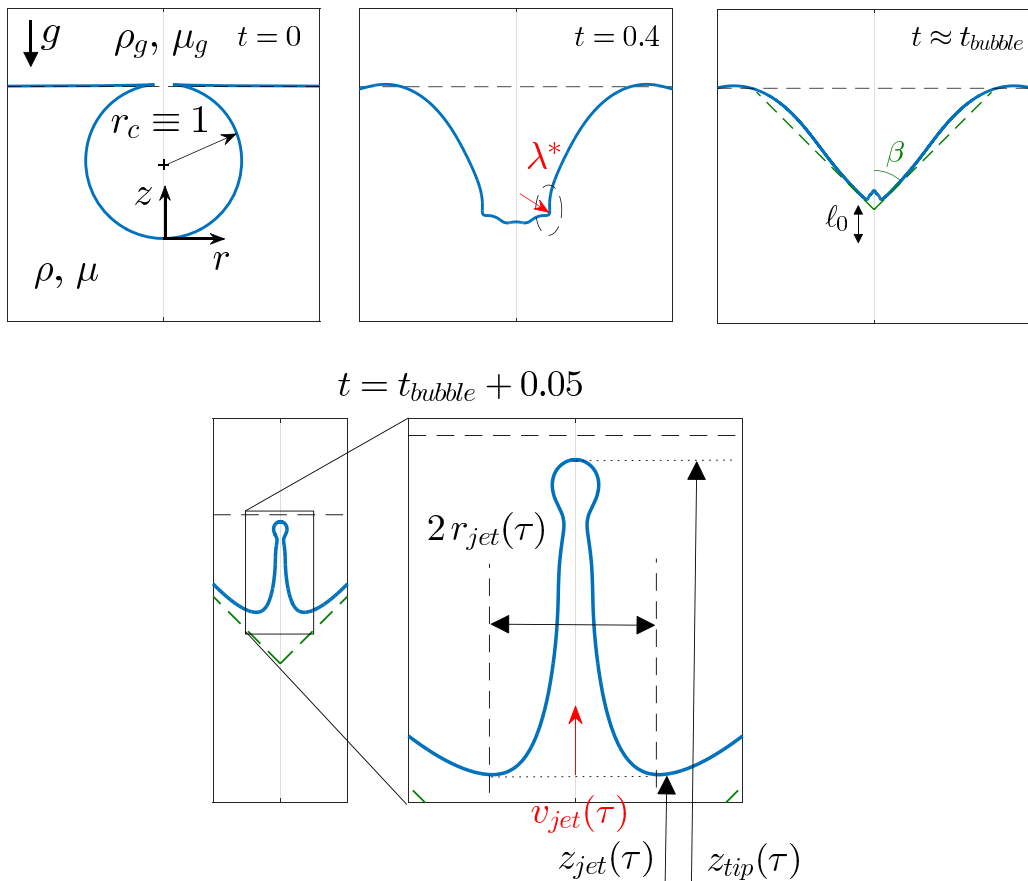


FIG. 1. Bubble collapse and subsequent jet ejection processes for $\text{La} = \text{Oh}^{-2} = 7200$ with r and z indicating the dimensionless radial and axial cylindrical coordinates. As we did in Ref. [49], the numerical simulations have been carried out for a value of the Bond number $\text{Bo} = 0.01$ and for fixed values of the density and viscosity ratios: $\rho_g/\rho = 1.2 \times 10^{-3}$ and $\mu_g/\mu = 1.8 \times 10^{-2}$ with ρ_g and μ_g indicating the gas density and viscosity. The last panel shows the base of the jet, which is the point at the interface $r = r_s(z, \tau)$ of coordinates $r = r_{\text{jet}}(\tau)$, $z = z_{\text{jet}}(\tau)$ where $\partial r_s/\partial z \rightarrow \infty$. The jet velocity is defined as $v_{\text{jet}}(\tau) = v_z(r = 0, z = z_{\text{jet}})$. The origin of times, $t = 0$, is set at the instant when the interface of the initially spherical bubble starts deforming and $t_{\text{bubble}}(\text{La})$ denotes the instant of time when the capillary wave reaches the bottom of the cavity; see Fig. 2(a)

by [32,49]:

$$r_{\text{jet}0}(\text{La}) = 0.2215 \left(1 - \sqrt{\frac{\text{Oh}}{0.0305}} \right), \quad (1)$$

where the dependence with $\text{Oh}^{1/2}$ comes from the fact that $\lambda^* \propto \text{Oh}^{1/2}$ [32]; note also that, for our subsequent purposes, it proves convenient to define here $r_{\text{jet}0}^* = r_{\text{jet}0}(\text{La} = 2500) \simeq 0.05$. It was shown in Ref. [49] and in Fig. 3 that the topology of the interface changes for $\text{La} < 2500$ since, in these cases, a tiny bubble is entrapped beneath the cavity before the jet is ejected; see Fig. 3. For $\text{La} < 2500$, the jet is also issued from the base of a truncated conical surface with a radius $r_{\text{jet}0}(\text{La} < 2500) < r_{\text{jet}0}^*$ and with an opening semiangle which verifies $\beta(\text{La} < 2500) < 45^\circ$; see Fig. 2(b) and Fig. 3 [51].

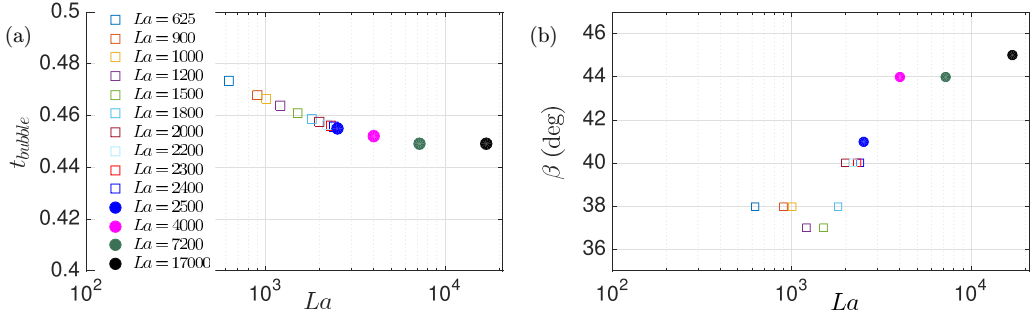


FIG. 2. (a) The values of t_{bubble} , with t_{bubble} the instant of time at which the capillary waves with a wavelength $\lambda^* \propto \text{Oh}^{1/2}$ reach the bottom of the cavity are almost independent of La because capillary waves propagate with a velocity which is independent of La [32]. (b) The value of the opening semiangle β depends on La : For $La \geq 2500$ a bubble is not entrapped beneath the bottom of the cavity and $\beta \approx 45^\circ$; for $La < 2500$, a satellite bubble is entrapped and $\beta < 45^\circ$; see Fig. 3 and the results in Fig. 1 of the Supplemental Material [48].

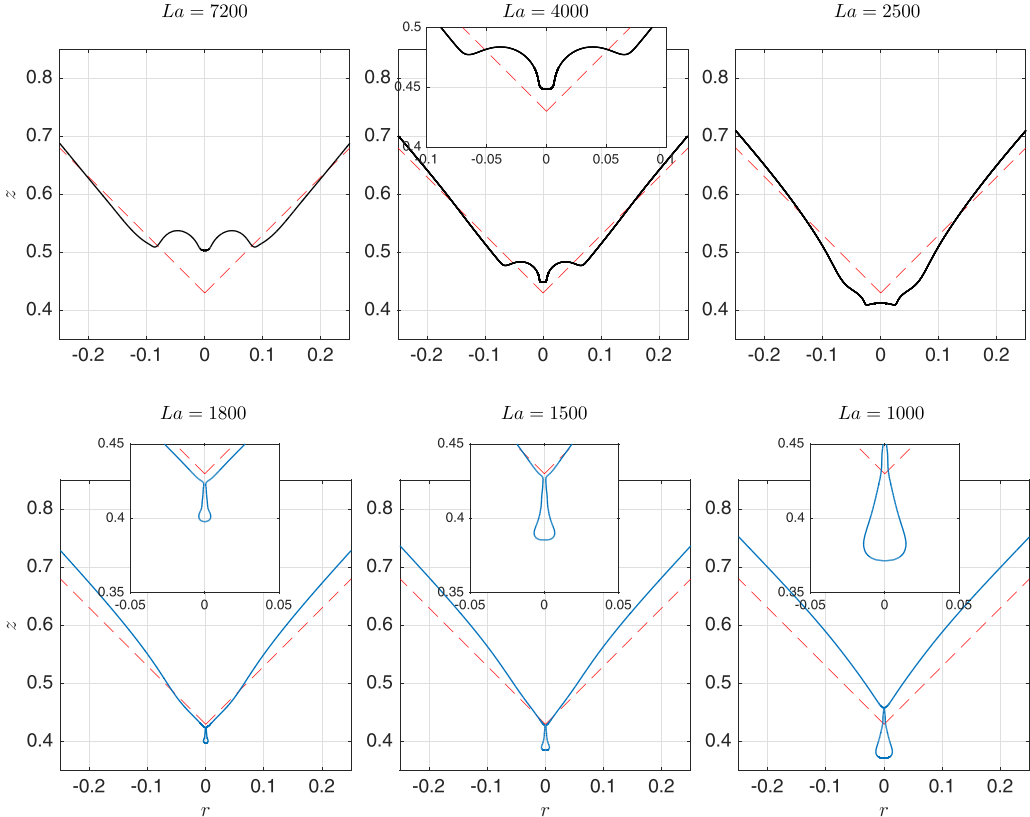


FIG. 3. Local shape of the cavity at the instant $t_{\text{bubble}}(La)$ the capillary waves reach the bottom of the bubble. Notice that, for $La \geq 2500$, a tiny satellite bubble is not entrapped beneath the cavity and the semiangle of the truncated conical surface from which the jet is ejected is very close to $\beta = 45^\circ$, with this angle being indicated in the figure using red dashed lines. In contrast, for $625 \lesssim La < 2500$, a satellite bubble is entrapped and $\beta \approx 37^\circ$ for $La \approx 1000$; see also Fig. 2(b).

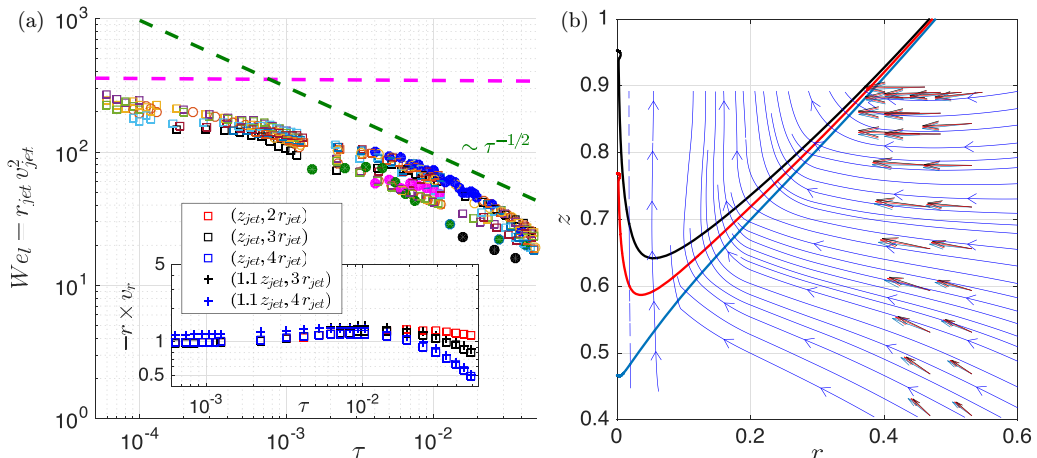


FIG. 4. (a) $We_l = r_{\text{jet}} v_{\text{jet}}^2 \gg 1$, with $We_l \propto \tau^{-1/2}$ for $\tau \gtrsim 10^{-3}$. Inset: The values of the radial flow rate per unit length calculated using GERRIS as $q = -r v_r$ for $La = 2400$ and different values of $r/r_{\text{jet}}(\tau)$ and $z/z_{\text{jet}}(\tau)$ remain nearly constant along two decades in time. (b) Streamlines calculated at $\tau = 10^{-5}$ and cavity shapes at three instants of time for $La = 1000$. The streamlines in the liquid are mostly horizontal at the side of the cavity walls, a fact indicating that the cavity collapse is driven by a radial velocity field. In contrast, the streamlines also reveal that the flow in the gas cavity is mostly directed along the axial direction. The velocity vectors plotted at two radial positions $r \approx 0.5$ at $\tau = 10^{-5}$ (blue), $\tau = 2.18 \times 10^{-3}$ (red), and $\tau = 4.18 \times 10^{-3}$ (black) do not change with time. The results in (b), together with the ones depicted in the inset of (a), indicate that the velocity field driving the jet ejection process *cannot* be approximated by the velocity field generated by a three-dimensional sink with a time-varying flow rate plus additional higher-order terms, a type of approximation which, however, can be used to model the velocity field *before* the jet is ejected; see Ref. [50] for details. In contrast, our results in Ref. [12] reveal that the axial velocity field at the bottom of the jets generated either after either a bubble bursts at a free interface or after a drop impacts a liquid pool, can be very well approximated by the flow generated by a line of sinks located at the axis of symmetry. In Ref. [12] we also show that the good agreement between predictions and the numerical results is kept along the whole time evolution of the jet.

The result for $We_l(\tau)$ in Fig. 4(a) show that (i) $We_l = v_{\text{jet}}^2 r_{\text{jet}} \gg 1$ for all values of $\tau > 0$, a fact already suggesting that the jet dynamics cannot be driven by capillary forces and (ii) We_l is far from being a constant since $We_l \propto \tau^{-1/2}$ for $\tau \gtrsim 10^{-3}$. These results indicate that bubble bursting jets cannot be described using the inertio-capillary solution of Refs. [35,36]. It could be argued that the result in Fig. 4(a) refers to magnitudes evaluated right at the base of the jet: However, our previous results in Refs. [15,49] reveal that the time evolution of the jet radius and of the jet velocity, and even the diameter and the velocity of the drops ejected, can be calculated in terms of the functions $r_{\text{jet}}(\tau)$, $z_{\text{jet}}(\tau)$, and $v_{\text{jet}}(\tau)$. Indeed, in Ref. [49], we coupled the ballistic equations deduced in Ref. [15], valid in the limit $We_l \gg 1$ of interest here [see Fig. 4(a)] with the mass and the momentum balances at the top drop, with this latter balance incorporating the relative flux of momentum, the capillary retraction term, and the drag force exerted by the gas, finding an excellent agreement between the numerical results and the predictions. Then, since $r_{\text{jet}}(\tau)$, $z_{\text{jet}}(\tau)$, and $v_{\text{jet}}(\tau)$ do not follow the inertio-capillary scaling in Refs. [35,36], as revealed by the results shown in Fig. 4(a), we can conclude that the jets emerging from the bursting of bubbles are not driven by balance between inertia and capillarity, as is claimed in Ref. [36]. In addition, Fig. 5 reveals that the scaled shapes of bubble-bursting jets superimpose onto the purely inertial, self-similar solution, found in Appendix A, which clearly differs from the inertio-capillary one reported in Ref. [36] because our new self-similar solution verifies the condition that the value of the far-field flow rate per unit length remains constant in time, a fact constituting an additional evidence

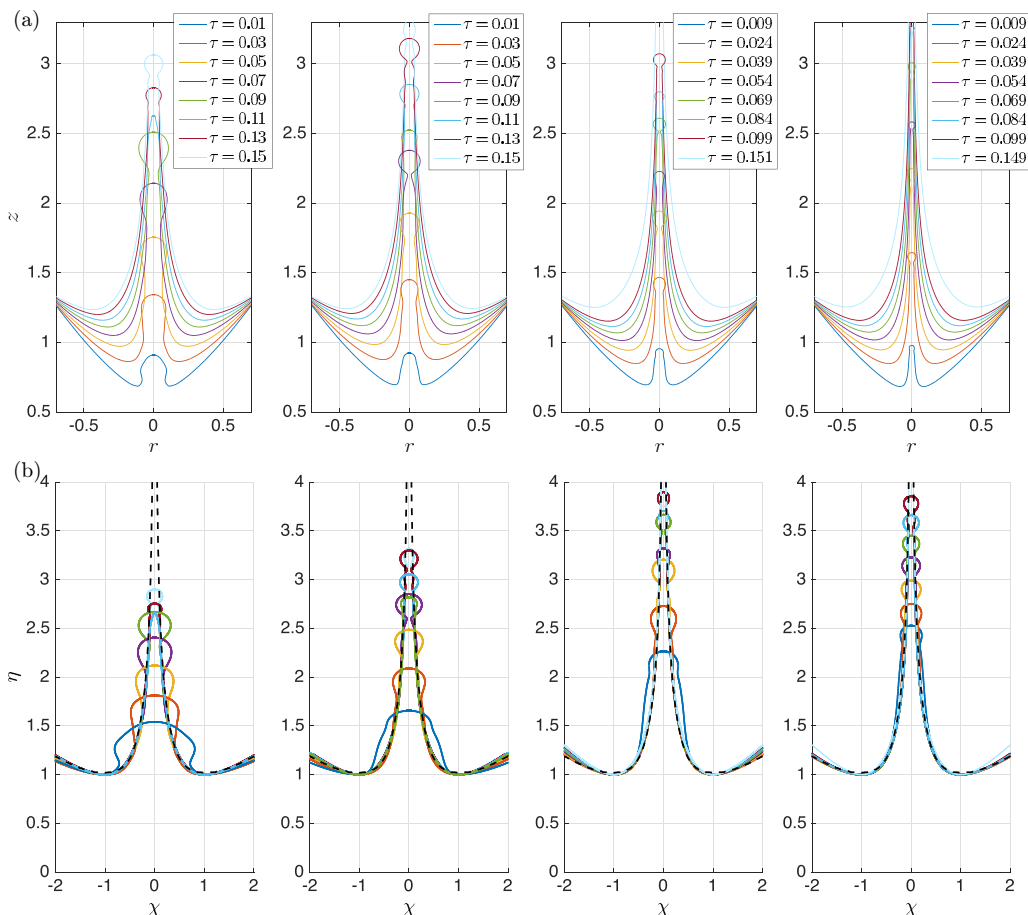


FIG. 5. The time-evolving jet shapes in the top row corresponding, from left to right, to $La = 17000$, $La = 7200$, $La = 4000$, and $La = 2500$, overlap onto the universal self-similar and purely inertial solution depicted in Fig. 16, represented here in dashed lines, for over a decade in time. Here $\chi = r/r_{\text{jet}}(\tau)$ and $\eta = (z - \ell_0)/(z_{\text{jet}}(\tau) - \ell_0)$, with $z - \ell_0$ representing the distance measured from the vertex of the cone with an opening semiangle $\beta \simeq 45^\circ$; see Figs. 1 and 3 and Appendix A.

supporting our description of the velocity field in terms of a line of sinks located at the axis of symmetry [12,32], as it will become even more clear in Sec. III.

In summary, the analytical results in Refs. [15,49] permit us to explicitly calculate the spatiotemporal evolutions of the jet shape and velocity, and even the sizes and the velocities of the drops ejected as a function of $r_{\text{jet}}(\tau)$, $z_{\text{jet}}(\tau)$, and $v_{\text{jet}}(\tau)$, this being the reason why the main purpose in this contribution is to deduce the equations governing the three time-dependent variables illustrated in Fig. 1.

In order to explain the results in Fig. 4(a), where it is shown that $We_l \propto \tau^{-1/2}$, we first review our previous results in Ref. [12], where we calculated the *initial* value of the jet velocity, $v_{\text{jet}0}(La)$, in terms of $r_{\text{jet}0}(La)$ given in Eq. (1) once the velocity field is expressed as the irrotational flow induced by a line of sinks with a flow rate per unit length $q_\infty \approx \text{const}$. In Ref. [12] we showed that, when the flow is induced by a line of sinks located at the axis of symmetry, the jet width and the jet velocity verify the equation

$$r_{\text{jet}}(\tau, La)v_{\text{jet}}(\tau, La) \propto q_\infty \quad (2)$$

with the value of q_∞ fixed during the initial cavity collapse process, namely before the jet is ejected [52]. Indeed, the capillary suction at the liquid side of the cavity induces a velocity V directed towards the axis of symmetry resulting from the balance $\rho V^2 \sim \sigma/R_b \Rightarrow V \propto V_c$ and, hence, the value of the far-field radial flow rate per unit length driving the collapse of the cavity is $Q_\infty \propto V_c R_b \rightarrow q_\infty \approx \text{const}$. It was explained in Refs. [12,15] that, once the radial inflow is set during the initial stage of the collapse, the value of q_∞ remains approximately constant in time for $\tau > 0$ because liquid inertia and mass conservation prevent appreciable changes in this quantity during the very short instants of time following the emergence of the jet. Our prediction for the velocity field in terms of a line of sinks with a constant value of q_∞ agrees very well with the numerical velocity field calculated at the base of the jet, as shown in Ref. [12] and, moreover, our description is further supported by (i) the result depicted in the inset of Fig. 4(a), where it is shown that the flow rate per unit length $q = -r v_r$ remains approximately constant in time for different values of $r/r_{\text{jet}}(\tau)$ and $z/z_{\text{jet}}(\tau)$, with v_r denoting the radial velocity, and by (ii) the results shown in Fig. 4(b), where it is seen that (a) the streamlines at the side of the cavity walls are horizontal and (b) the velocity does not appreciably changes with time for a fixed value of r .

Before proceeding to deduce in the next section the equations for the time-dependent functions $r_{\text{jet}}(\tau)$, $z_{\text{jet}}(\tau)$, and $v_{\text{jet}}(\tau)$ up to prefactors, in the following we briefly explain the reason behind the result in Fig. 4(a), which shows that $\text{We}_l \propto \tau^{-1/2}$ for $\tau \gtrsim 3 \times 10^{-3}$.

In order to calculate both $r_{\text{jet}}(\tau, \text{La})$ and $v_{\text{jet}}(\tau, \text{La})$, we need to add to Eq. (2) a relationship for $z_{\text{jet}}(\tau)$, defined in Fig. 1, which we combine with the equation $v_{\text{jet}} = 2 dz_{\text{jet}}/d\tau$: Indeed, since $\text{We}_l \gg 1$, the liquid pressure remains approximately constant at the portion of the interface surrounding the base of the jet. Hence, by virtue of the Euler-Bernoulli equation expressed in a frame of reference moving vertically with a velocity $dz_{\text{jet}}/d\tau$, the modulus of the velocity remains constant and equal to $dz_{\text{jet}}/d\tau$ along the interface and, since the direction of the velocity is reversed in the moving frame of reference at the jet base we conclude that, in the laboratory frame of reference, $v_{\text{jet}}(\tau) = 2 dz_{\text{jet}}/d\tau$; see also Sec. III. The remaining equation for z_{jet} can be understood in simple terms taking into account that $z_{\text{jet}}(\tau)$ is located, for each value of τ , at the vertical position where the interface $r = r_s(z, \tau)$ meets the axis of symmetry, $r = 0$. Indeed, the integration of the kinematic boundary condition yields to

$$\frac{dr_s}{d\tau} \propto -\frac{q_\infty}{r_s} \Rightarrow r_s^2(z, \tau) - (z \tan \beta)^2 \propto -2q_\infty \tau, \quad (3)$$

where we have taken into account that $v_r \simeq -q_\infty/r$ and that $r_s(z, \tau = 0) = z \tan \beta$; see Fig. 1. Then $z_{\text{jet}}(\tau)$ is deduced making $r_s(z_{\text{jet}}(\tau), \tau) = 0$ in Eq. (3), from which it follows that $z_{\text{jet}} \propto \sqrt{q_\infty \tau} / \tan \beta \Rightarrow v_{\text{jet}}(\tau) \propto dz_{\text{jet}}/d\tau \propto \sqrt{q_\infty/\tau} / \tan \beta$. Hence, by virtue of the mass balance, Eq. (2), $r_{\text{jet}}(\tau) \propto \tan \beta \sqrt{q_\infty \tau}$ and, consequently, $\text{We}_l = r_{\text{jet}} v_{\text{jet}}^2 \propto \tau^{-1/2}$, explaining the result depicted in Fig. 4(a).

The scalings in the paragraph above are properly quantified in the next section.

III. A THEORY ON THE EJECTION OF JETS FROM COLLAPSING CAVITIES

The results in Sec. II reveal that the bursting of a bubble with a radius $R_b \ll \sqrt{\sigma/(\rho g)}$, with g indicating the gravitational acceleration in a liquid of density ρ , viscosity μ , and interfacial tension coefficient σ , can be described in terms of a two-stage process characterized by an initial acceleration stage where the pressure difference $\Delta p \propto \sigma/R_b$ induces a mostly radial velocity field characterized by a value of the flow rate per unit length given by

$$Q_\infty \propto V_c R_b \quad \text{with} \quad \rho V_c^2 \sim \Delta p \Rightarrow Q_\infty \propto R_b \left(\frac{\Delta p}{\rho} \right)^{1/2}. \quad (4)$$

The flow rate Q_∞ in Eq. (4) remains mostly constant in time along the second stage, during which the jet is issued, because liquid inertia and mass conservation prevent appreciable changes of this quantity during the very short timescale characterizing the jet ejection process [12,15]. Clearly,

the previous description of the flow can also be applied to other similar physical situations where the initial acceleration stage is induced by either the hydrostatic pressure difference $\Delta p \sim \rho g R_b$ and, hence, $Q_\infty \propto R_b \sqrt{g R_b}$ [19] or by the jump between the liquid and vapor pressures, namely $\Delta p \sim p_a - p_v$, from which it follows that $Q_\infty \propto R_b [(p_a - p_v)/\rho]^{1/2}$ [2,28].

Then, in order to describe the ejection of jets produced by the implosion of cavities triggered by the radial flow of a liquid which has been previously accelerated towards the axis of symmetry by the pressure difference Δp , here we will analyze the collapse of an axisymmetric bubble or cavity like the ones sketched in Figs. 6(a) and 6(b) under the incompressible approach. The flow rate per unit length Q_∞ which is established during the initial acceleration process, remains constant in time and acts as the far-field boundary condition driving the ejection of the jet because it forces the inward motion of the cavity walls and, therefore, the jet is issued as a mere consequence of mass conservation.

We then consider the axisymmetric bubble or cavity sketched in Figs. 6(a) and 6(b) of characteristic length L_c filled with a gas of density ρ_g and viscosity μ_g whose collapse is driven by a far-field radial flow characterized by the velocity V_c . Using L_c , L_c/V_c , and ρV_c^2 as the characteristic scales of length, time, and pressure, the physical situation under study here and sketched in Figs. 6(a) and 6(b) can be described in terms of the following dimensionless parameters:

$$\text{We} = \frac{\rho V_c^2 L_c}{\sigma}, \quad \text{Re} = \frac{\rho V_c L_c}{\mu}, \quad m = \frac{\mu_g}{\mu}, \quad \Lambda = \frac{\rho_g}{\rho}. \quad (5)$$

As in Sec. II, dimensionless variables will be written using lowercase letters to differentiate them from their dimensional counterparts, written in capitals, r and z will respectively indicate the dimensionless radial and axial spatial coordinates in a cylindrical coordinate system, and τ will indicate the dimensionless time after the jet is ejected. In Sec. II, $L_c = R_b$, with R_b indicating the initial radius of the spherical bubble and $V_c = \sqrt{\sigma/(\rho R_b)}$ is the so-called capillary velocity. Therefore, for the case of bubble bursting jets considered in Sec. II, $\text{We} = 1$ and $\text{Re} = \text{Oh}^{-1}$, with $\text{Oh} = \mu/\sqrt{\rho R_b \sigma}$ the so-called Ohnesorge number, which must be such that $\text{Oh} \ll 1$ for a jet to be ejected from the bottom of the collapsing bubble [49]. As was also pointed out above, for the case of jets ejected as a consequence of the gravitational collapse of a bubble of length H , $L_c = H$ and $V_c = \sqrt{gH}$ [19], and, for the case of the cavitation of a bubble of radius R_b considered in Ref. [28], $L_c = R_b$ and $V_c = [(p_a - p_v)/\rho]^{1/2}$. The results in Sec. II show the relevance played by the two time-dependent functions $z_{\text{jet}}(\tau)$ and $r_{\text{jet}}(\tau)$ characterizing the position of the interface of equation $r - r_s(z, \tau) = 0$ in the description of the jet dynamics; see Figs. 6(c) and 6(d). Then, it will be our main purpose here to find analytical expressions for $r_{\text{jet}}(\tau)$, $v_{\text{jet}}(\tau)$, and $z_{\text{jet}}(\tau)$ in the limit $\tau \ll 1$.

The results in Sec. II indicate that $r_{\text{jet}} \propto \sqrt{q_\infty \tau}$ and $v_{\text{jet}} \propto dz_{\text{jet}}/d\tau \propto \sqrt{q_\infty/\tau}$ when the collapse of a conical cavity of semiangle β (see Figs. 6 and 13) is driven by a far-field boundary condition expressing that q_∞ remains constant in time. Hence, the value of the local Reynolds number characterizing the flow at the base of the jet, $\text{Re}_l = \text{Oh}^{-1} v_{\text{jet}} r_{\text{jet}} \propto \text{Oh}^{-1}$, will remain constant in time and the value of the local Weber number will diverge as $\text{We}_l = v_{\text{jet}}^2 r_{\text{jet}} \propto \tau^{-1/2} \gg 1$ in the limit $\tau \ll 1$ of interest here; see Sec. II. Then, provided that the Reynolds number at the scale of the bubble is large, i.e., provided that $\text{Oh}^{-1} \gg 1$ for the case considered in Sec. II, both capillary and viscous effects can be neglected, an approximation which is further supported by the numerical results presented in Appendix A. Moreover, since we will not consider the effects of the gas on the jet ejection process, the solutions to be deduced next will not depend on any of the dimensionless parameters defined in Eq. (5); however, as will be shown below, our results will strongly depend on the value of the dimensionless flow rate per unit length q_∞ and on the initial geometry of the cavity, i.e., on the function $r_s(z, \tau = 0)$.

Consequently, since in view of the discussion in the paragraphs above, viscous and capillary effects can be neglected, we consider here the case of an incompressible flow in which vorticity is zero, enabling us to express the velocity field in terms of a velocity potential ϕ , i.e., $\mathbf{v} = \nabla\phi$, with

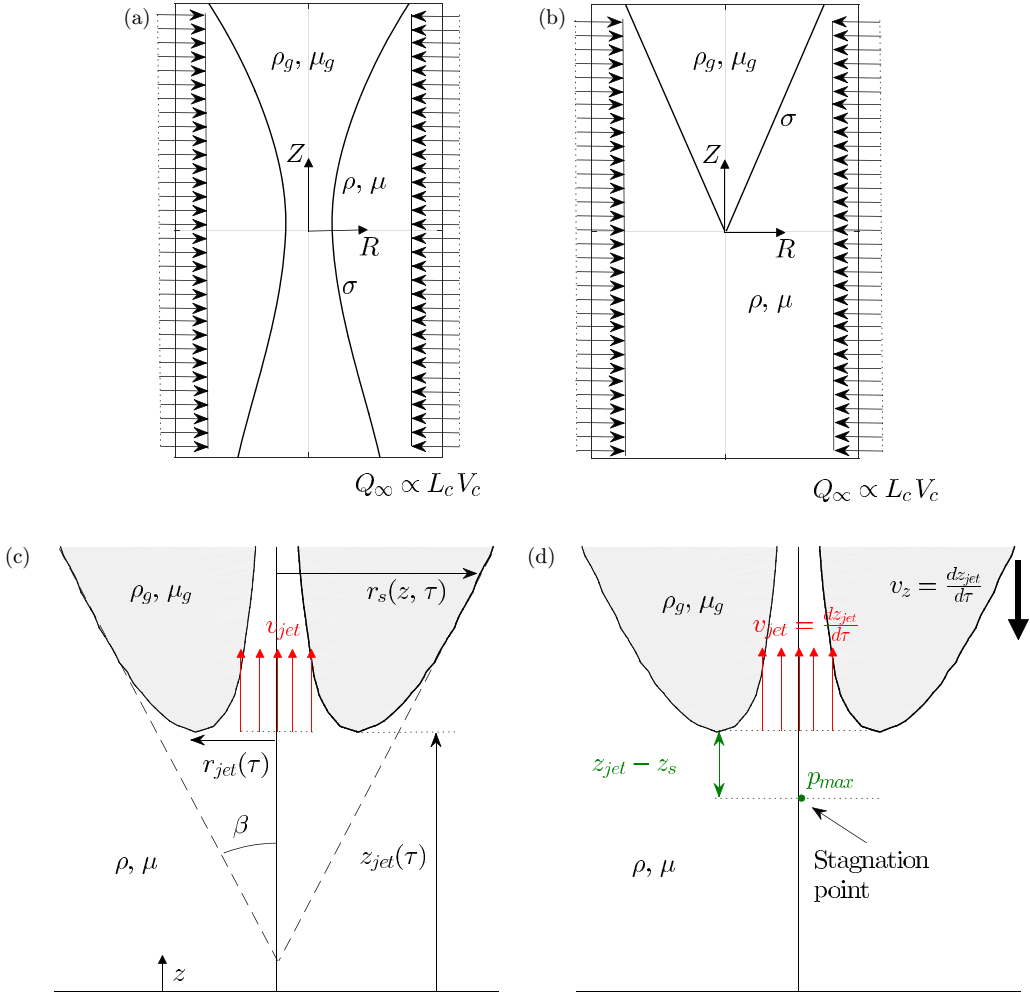


FIG. 6. [(a) and (b)] Sketches showing the collapse of cavities with different shapes and with characteristic lengths L_c that implode as a consequence of an imposed far-field radial velocity field such that the flow rate per unit length $Q_\infty \propto V_c L_c$ remains constant in time. (c) Sketch illustrating the definitions of the time-dependent variables used to analyze the jet ejection process: The interface is located at $r = r_s(z, \tau)$, the base of the jet is the point at the interface of coordinates $r = r_{jet}(\tau)$, $z = z_{jet}(\tau)$, where $\partial r_s / \partial z \rightarrow \infty$, and the jet velocity is defined as $v_{jet}(\tau) = v_z(r = 0, z = z_{jet} + \alpha r_{jet})$ with $\alpha \sim 1$ being $z = z_{jet}(\tau) + \alpha r_{jet}(\tau)$ the vertical coordinate within the jet where the pressure approximately relaxes to that of the gas. (d) Sketch of the flow in a frame of reference moving vertically with the velocity $dz_{jet}/d\tau$. In this frame of reference, there exists a stagnation point of the flow located at a distance from the base of the jet $z_{jet} - z_s \propto r_{jet}(\tau)$, where the pressure is maximum and is equal to $p_{max}(\tau)$.

ϕ satisfying the Laplace equation $\nabla^2 \phi = 0$. We then analyze, at short times, $\tau \ll 1$, the implosion of an axisymmetric cavity, symmetric with respect to the plane $z = 0$, which collapses forced by a far-field boundary condition of the type illustrated in Fig. 7; see also Figs. 6 and 13,

$$r \frac{\partial \phi}{\partial r} = -q_\infty \quad \text{for } r \rightarrow \infty. \quad (6)$$

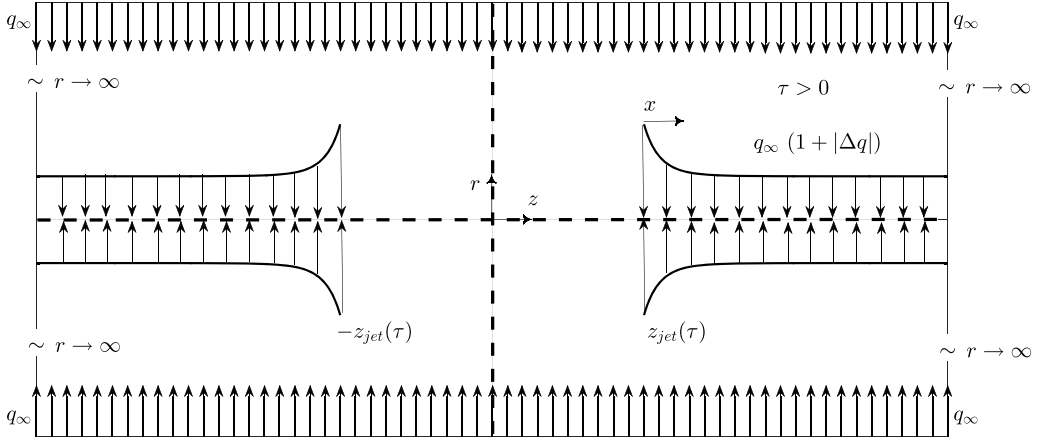


FIG. 7. The sketch illustrates that, for instants of time $\tau \ll 1$, the irrotational velocity field satisfying the boundary conditions in Eqs. (6) and (7) is a line of sinks of intensity $q_\infty[1 + |\Delta q(z, \tau)|]$ extending along the axis in the region $|z| > z_{\text{jet}}(\tau)$ with $q_\infty \Delta q(z, \tau)$ such that $\partial\phi/\partial z = 0$ at $r = r_s(z \geq z_{\text{jet}}(\tau), \tau) \simeq 0$ since $r_s \ll 1$; see Eqs. (8)–(11).

We also consider that the cavity is slender, i.e., the position of the interface satisfies $r_s(z, \tau) \ll 1$ and $\partial r_s/\partial z \ll 1$. Before the jet is ejected, namely for instants of time $\tau < 0$, the irrotational velocity field satisfying the boundary condition (6) is the one generated by a line of sinks of intensity q_∞ located at the axis of symmetry. Due to the fact that the cavity is slender, the velocity field produced by the line of sinks at the axis is, in a first approximation, normal to the interface and, therefore, the potential at $\tau = 0^+$, which is when the jet is first issued, can be set to $\phi = \text{const}$ at $r = r_s(z, \tau = 0^+)$. As it is sketched in Fig. 7, once the two symmetrical jets are ejected from $z = \pm z_{\text{jet}}(\tau)$ for instants of time $\tau > 0$, the free interface disappears along the region $|z| < z_{\text{jet}}(\tau)$ and two symmetric jets are ejected from $z = \pm z_{\text{jet}}(\tau)$. Consequently,

$$r \frac{\partial \phi}{\partial r}(r = 0, z, \tau) = 0 \quad \text{for} \quad |z| < z_{\text{jet}}(\tau) \quad \text{and} \quad \tau > 0, \quad (7)$$

since, otherwise, the liquid velocity would tend to infinity at the axis. Hence, the irrotational and incompressible velocity field satisfying the boundary conditions (6) and (7) is the one induced by a line of sinks with intensities $q_\infty[1 + |\Delta q(z, \tau)|]$ extending along $|z| \geq z_{\text{jet}}(\tau)$; see Fig. 7. In order to determine the unknown function $\Delta q(z, \tau)$ we describe the “impact” of an axisymmetric flow over $r = 0$, which shares similarities with the free boundary problem of Wagner type that needs to be solved, for instance, in order to quantify the impact of two-dimensional solids with small deadrise angles over free surfaces [53–55]. Indeed, notice that the integration in time of the Euler-Bernoulli equation (A5) permits us to conclude that, for $\tau \ll 1$, $\phi \simeq \text{const}$ at $r = r_s(z, \tau) \ll 1$ for $|z| \geq z_{\text{jet}}(\tau)$ because at $\tau = 0^+$ $\phi = \text{const}$ at the free interface and $\tau |\nabla \phi|^2/2 \rightarrow 0$ as $\tau \rightarrow 0$. Moreover, since $r_s \ll 1$, this boundary condition for the Laplace equation can be linearized by retaining only the first term in the Taylor series expansion of ϕ around $r = 0$, which yields the following boundary condition for $\partial\phi/\partial z$ at $r = 0$:

$$\phi(r = 0, z, \tau) = \text{const} \Rightarrow \frac{\partial \phi}{\partial z}(r = 0, z, \tau) = 0 \quad \text{for} \quad |z| \geq z_{\text{jet}}(\tau), \quad (8)$$

a condition also expressing that, in the limit of slender cavities of interest here, velocities are normal to the interface. Now notice that the solution of the Laplace equation $\nabla^2 \phi = 0$ subjected to the boundary conditions (6)–(8) is a distribution of sinks with intensity q_∞ located at the axis of symmetry and extending along $|z| < \infty$, plus a line of sources of intensity q_∞ that extends along

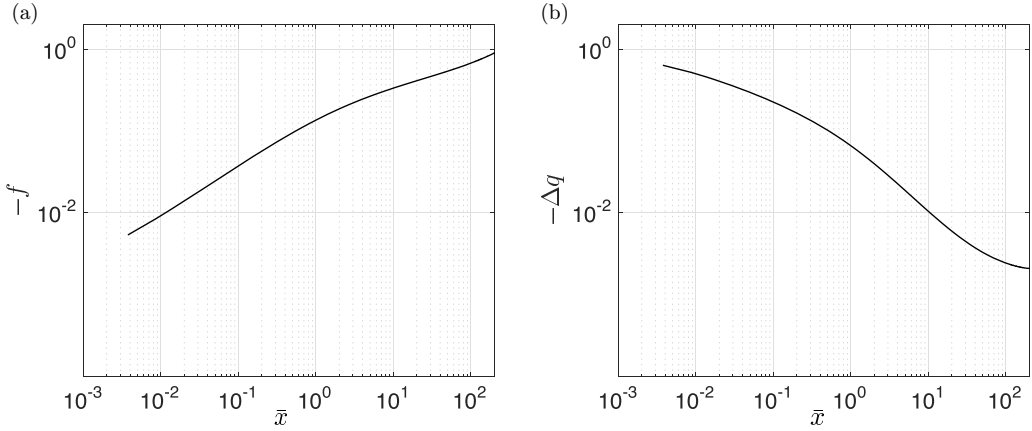


FIG. 8. (a) The function $f(\bar{x})$, with $\bar{x} = \bar{z} - 1$, such that $f(\bar{x} = 0) = 0$ and $f(\bar{x} \rightarrow \infty) \rightarrow -1$ is calculated solving the integral equation (11) using the numerical code provided in Appendix B (see also the Supplemental Material [48]). (b) The function $\Delta q(\bar{x}) = df/d\bar{x}$ is such that $-\Delta q(\bar{x} \rightarrow 0) \rightarrow 0.7$.

the axis in the region $|z| < z_{\text{jet}}(\tau)$, plus a line of sinks with a strength $q_{\infty} \Delta q(z, \tau)$ that extends along the axis in the region $|z| \geq z_{\text{jet}}(\tau)$. Notice that the distribution $q_{\infty} \Delta q(z, \tau)$ is needed in order to preserve the flow rate per unit length imposed by the far-field boundary condition (6) and to compensate the flow rate which is not suctioned through the axis along the region $|z| < z_{\text{jet}}$. Hence $\Delta q(z, \tau)$ is determined from the solution of the integral equation that results from imposing the boundary condition expressed by Eq. (8):

$$\int_{-z_{\text{jet}}}^{z_{\text{jet}}} \frac{(z - z_0) dz_0}{[(z - z_0)^2]^{3/2}} + \int_{z_{\text{jet}}}^{\infty} \frac{\Delta q(z_0)(z - z_0) dz_0}{[(z - z_0)^2]^{3/2}} + \int_{-\infty}^{-z_{\text{jet}}} \frac{\Delta q(-z_0)(z - z_0) dz_0}{[(z - z_0)^2]^{3/2}} = 0. \quad (9)$$

The first integral in Eq. (9) corresponds to the axial velocity generated at $r = 0$ and $z > z_{\text{jet}}(\tau)$ by the line of sources of intensity q_{∞} located at $|z| < z_{\text{jet}}$, whereas the second and third integrals correspond to the axial velocities at $r = 0$ generated by the distribution of sinks of intensity $q_{\infty} \Delta q(z, \tau)$ located at $|z| \geq z_{\text{jet}}$; see the sketch in Fig. 7. Notice that the contribution of the third integral is rather small when compared with that of the second integral in Eq. (9), this being the reason why this term will be neglected in what follows.

In order to solve the integral equation for Δq , we first notice that, in terms of the variables

$$\bar{z} = \frac{z}{z_{\text{jet}}(\tau)}, \quad \bar{z}_0 = \frac{z_0}{z_{\text{jet}}(\tau)}, \quad \Delta q = \frac{df}{d\bar{z}} \quad (10)$$

with $f(\bar{z} = 1) = 0$, the integral equation (9) reads:

$$\frac{1}{\bar{z} - 1} - \frac{1}{\bar{z} + 1} + \int_1^{\infty} \frac{df/d\bar{z}_0(\bar{z} - \bar{z}_0) d\bar{z}_0}{[(\bar{z} - \bar{z}_0)^2]^{3/2}} = 0. \quad (11)$$

Equation (11) is solved numerically using the method detailed in Appendix B, and the resulting functions f and Δq are represented in Fig. 8, where it is also shown that $-\Delta q(\bar{z} \rightarrow 1) \approx 0.7$. Let us point out here that the predicted sink distribution $q_{\infty}(1 + |\Delta q|)$ with Δq given in Fig. 8 is compared in Fig. 17 with the results of full numerical simulations of the type described in Appendix A, finding good agreement between the theoretical and the numerical results. Once Δq is known, the equation for $z_{\text{jet}}(\tau)$ is deduced following the same ideas as those in Refs. [53,55,56], namely making use of the kinematic boundary condition at the interface and considering that the jet root is

TABLE I. The table provides the numerical values of the integral in Eq. (15) for different values of n using the values of $\Delta q(\bar{x})$ depicted in Fig. 3.

	$n = 2$	$n = 3$	$n = 4$	$n = 5$	$n = 6$	$n = 8$	$n = 10$
$1 + n \int_0^\infty \Delta q(\bar{x}) /(1 + \bar{x})^{(n+1)} d\bar{x}$	1.14	1.18	1.20	1.20	1.24	1.24	1.30

located at the position where the interface meets the axis of symmetry:

$$\frac{dr_s}{d\tau} = v_r(r = r_s) = -q_\infty \frac{1 + |\Delta q|}{r_s} \Rightarrow -\frac{r_s^2(z = z_{\text{jet}})}{2q_\infty} = -\tau - \int_0^\tau |\Delta q[z = z_{\text{jet}}(\tau)]| d\tau'. \quad (12)$$

At an instant of time $\tau' \leq \tau$ and for a fixed value of $z_{\text{jet}}(\tau)$, we define

$$\bar{x} = z_{\text{jet}}(\tau)/z'_{\text{jet}} - 1 \quad \text{with} \quad z'_{\text{jet}} = z_{\text{jet}}(\tau') \quad (13)$$

and, therefore, the integral equation (12) can be written as

$$-\frac{r_s^2(z = z_{\text{jet}})}{2q_\infty} = -\tau - \int_\infty^0 |\Delta q(\bar{x})| \frac{d\tau'}{dz'_{\text{jet}}} \frac{dz'_{\text{jet}}}{d\bar{x}} d\bar{x}. \quad (14)$$

Equation (14) can be solved using a procedure similar to that followed in Ref. [56], where we considered the analogous case of the impact of a spherical drop over a wall: Indeed, for the case of axisymmetric cavities with equations of the type $r_s^2(z = z_{\text{jet}}) = 2C^{-1}z_{\text{jet}}^n$ with C an arbitrary constant, the solution of Eq. (14) is of the form $\tau = A^{-1}z_{\text{jet}}^n$ and, consequently,

$$\begin{aligned} -\frac{r_s^2(z = z_{\text{jet}})}{2q_\infty} &= -\frac{2C^{-1}z_{\text{jet}}^n}{2q_\infty} = -\tau - \int_\infty^0 -|\Delta q(\bar{x})| nA^{-1}(z'_{\text{jet}})^{(n-1)} \frac{z_{\text{jet}}^2}{z_{\text{jet}}(\tau)} d\bar{x} \\ &= -A^{-1}z_{\text{jet}}^n - nA^{-1}z_{\text{jet}}^n \int_0^\infty \frac{|\Delta q(\bar{x})|}{(1 + \bar{x})^{n+1}} d\bar{x} \Rightarrow A \\ &= Cq_\infty \left[1 + n \int_0^\infty \frac{|\Delta q(\bar{x})|}{(1 + \bar{x})^{n+1}} d\bar{x} \right] \Rightarrow \\ z_{\text{jet}} &= \left[1 + n \int_0^\infty \frac{|\Delta q(\bar{x})|}{(1 + \bar{x})^{n+1}} d\bar{x} \right]^{1/n} (Cq_\infty \tau)^{1/n}, \end{aligned} \quad (15)$$

where we have made use of Eq. (13). Notice that the values of the integral $\int_0^\infty |\Delta q|/(1 + \bar{x})^{(n+1)} d\bar{x}$, which can be calculated numerically for different values of n using the function $\Delta q(\bar{x})$ depicted in Fig. 8, are given in Table I. Once $z_{\text{jet}}(\tau)$ is calculated through Eq. (15), the jet velocity in the laboratory frame of reference, v_{jet} , is calculated expressing the Euler-Bernoulli equation in a relative frame of reference moving with the jet base velocity, $dz_{\text{jet}}/d\tau$. Indeed, the numerical results in Fig. 9(a), which correspond to the type of numerical simulations detailed in Appendix A indicate that, in the moving frame of reference, the free surface is a streamline along a vertical distance $\sim r_{\text{jet}}$ pointing upwards from the base of the jet and that the stagnation point of the flow is located at a distance $\sim r_{\text{jet}}(\tau)$ below the base of the jet; see also Fig. 6. Moreover, Fig. 9(a) reveals that the jet is fed from a narrow region of width $\sim r_{\text{jet}}(\tau)$ located nearby the free interface, a result which was already noticed in Ref. [37] experimentally and in Ref. [14] numerically. In addition, Fig. 9(b) shows that the jet shapes corresponding to different instants of time superimpose onto a single curve when rescaled using $r_{\text{jet}}(\tau)$ as the characteristic length scale, whereas Fig. 9(c) shows the values of the rescaled pressure evaluated at the axis of symmetry along the spatial region $z - z_{\text{jet}}(\tau) \sim r_{\text{jet}}(\tau)$ for different instants of time. Figure 9(c) reveals that the stagnation point of the flow is indeed located at a distance $\sim r_{\text{jet}}$ below the base of the jet and that the liquid pressure relaxes to that of the gas, p_{gas} ,

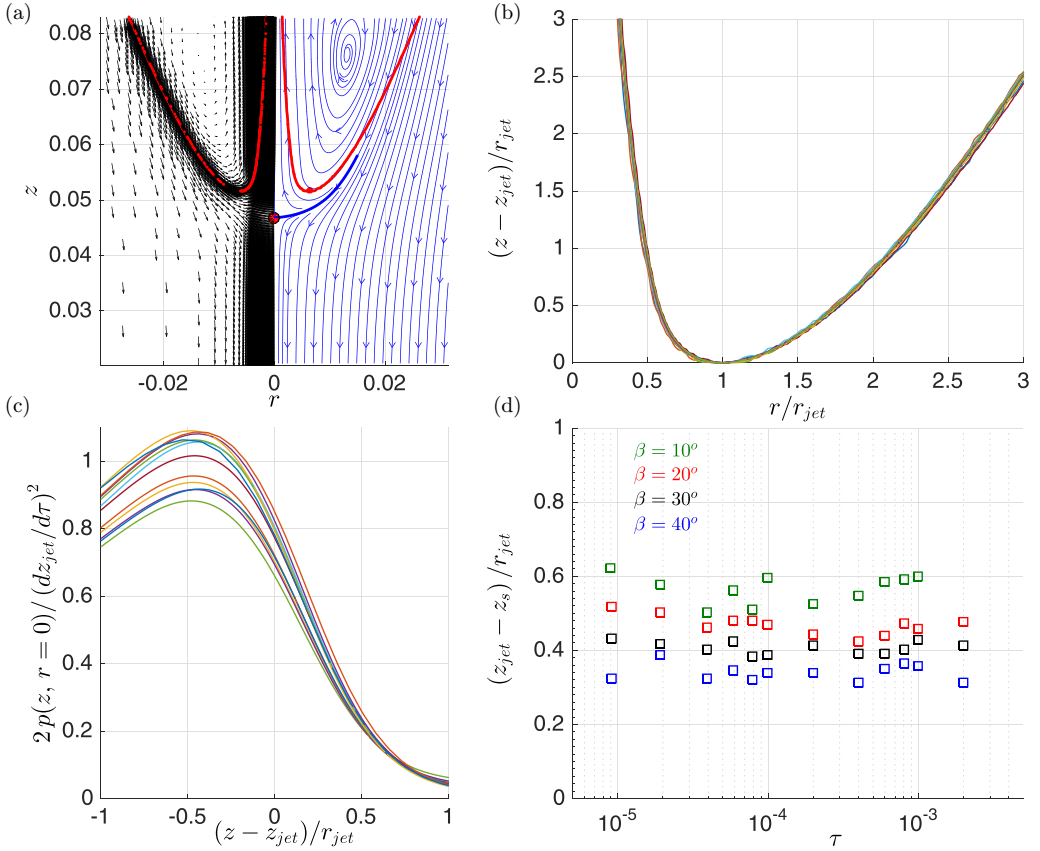


FIG. 9. (a) Streamlines corresponding to a conical cavity with an opening semiangle of $\beta = 20^\circ$ (see Appendix A for numerical details) represented at a generic instant τ_0 in a frame of reference moving vertically with the velocity $dz_{\text{jet}}/d\tau(\tau_0)$. The thick blue line represents the dividing streamline. (b) When scaled using $r_{\text{jet}}(\tau)$, the jet shapes corresponding to $\beta = 20^\circ$ superimpose onto a single curve for over two decades in time. (c) Scaled pressure at the axis of symmetry in a region surrounding the base of the jet for over two decades in time, here $\beta = 20^\circ$. Pressures are scaled in terms of the value of the stagnation pressure in the moving frame of reference, $1/2(dz_{\text{jet}}/d\tau)^2$. (d) Time evolution of the location of the stagnation point of the flow in the moving frame of reference. Green, red, black, and blue squares indicate, respectively, the results corresponding to conical cavities with opening semiangles $\beta = 10^\circ$, 20° , 30° , and 40° ; see Appendix A for numerical details.

at $z \simeq z_{\text{jet}}(\tau) + r_{\text{jet}}(\tau)$. Therefore, since the jet is slender and capillary effects are subdominant, the pressure in the liquid will remain, in a first approach, constant for $z \gtrsim z_{\text{jet}}(\tau) + r_{\text{jet}}(\tau)$, this fact meaning that both the jet shape and the velocity within the spatiotemporal region (z, τ) , with $z \gtrsim z_{\text{jet}}(\tau) + r_{\text{jet}}(\tau)$, can be predicted using the ballistic equations deduced in Ref. [15]. Figure 9(c) also shows that the maximum pressure p_{max} is the stagnation pressure, with this value being attained at the point where the dividing streamline meets the axis of symmetry; see Fig. 9(a). Hence, p_{max} can be calculated using the Euler-Bernoulli equation in the moving frame of reference as

$$p_{\text{max}} - p_{\text{gas}} \simeq \frac{1}{2} \left(\frac{dz_{\text{jet}}}{d\tau} \right)^2, \quad (16)$$

because the modulus of the upstream velocity in the moving frame of reference at the dividing streamline is $\approx dz_{\text{jet}}/d\tau$ and the pressure upstream the dividing streamline, which is in close proximity to the free surface, is that of the gas because capillary effects are negligible. Therefore,

taking into account that the flow field is quasisteady in a region of width $\sim r_{\text{jet}}(\tau)$ surrounding the base of the jet and making use of the Euler-Bernoulli equation along a streamline connecting the stagnation point of the flow in the relative frame of reference and the downstream position within the jet where the pressure relaxes to that of the gas, we find that

$$p_{\text{max}} - p_{\text{gas}} \simeq \frac{1}{2} \tilde{v}_{\text{jet}}^2 \quad \text{with} \quad \tilde{v}_{\text{jet}} = v_z(r=0, z = z_{\text{jet}} + r_{\text{jet}}) - \frac{dz_{\text{jet}}}{d\tau}, \quad (17)$$

indicating the axial velocity in the moving frame of reference. Consequently, making use of Eq. (16) we conclude that the jet velocity in the laboratory frame of reference at the axial coordinate z where the liquid pressure relaxes to that of the gas is given by

$$v_{\text{jet}}(\tau) = v_z(r=0, z = z_{\text{jet}} + r_{\text{jet}}) = 2 \frac{dz_{\text{jet}}}{d\tau}. \quad (18)$$

Finally, the result in Fig. 9(d) indicates that the maximum value of the pressure, namely the stagnation pressure in the moving frame of reference [see also the sketch in Fig. 6(d)], is reached at a distance from the base of the jet $z_{\text{jet}}(\tau) - z_s(\tau)$, such that the ratio $[z_{\text{jet}}(\tau) - z_s(\tau)]/r_{\text{jet}}(\tau) \sim O(1)$ remains approximately constant in time.

Then, making use of Eqs. (15) and (18), we conclude that the velocity within the jet at the location where the liquid pressure relaxes to that of the gas, namely at $z = z_{\text{jet}}(\tau) + \alpha r_{\text{jet}}(\tau)$ with $\alpha \simeq 1$, is

$$v_{\text{jet}} \simeq 2 \frac{dz_{\text{jet}}}{d\tau} \simeq \frac{2Cq_{\infty}}{n} \left[1 + n \int_0^{\infty} \frac{|\Delta q(\bar{x})|}{(1+\bar{x})^{n+1}} d\bar{x} \right]^{1/n} (Cq_{\infty}\tau)^{(1-n)/n}. \quad (19)$$

The particularization of Eqs. (15) and (19) to the case of conical cavities with an equation of the form $r_s = z \tan \beta$, ($C = 2/\tan^2 \beta$) yields

$$z_{\text{jet}} = \left[1 + 2 \int_0^{\infty} \frac{|\Delta q(\bar{x})|}{(1+\bar{x})^3} d\bar{x} \right]^{1/2} (2q_{\infty}\tau/\tan^2 \beta)^{1/2} \simeq \frac{1.5}{\tan \beta} \sqrt{q_{\infty}\tau} \quad (20)$$

and

$$v_{\text{jet}} \simeq 2 \frac{dz_{\text{jet}}}{d\tau} \simeq \frac{1.5}{\tan \beta} \sqrt{\frac{q_{\infty}}{\tau}}, \quad (21)$$

where we have made use of the value of the integral given in Table I corresponding to $n = 2$. For the analogous case of parabolic cavities with an equation of the form $r_s = z^2/(2r_c)$, Eqs. (15) and (19) yield the following expressions for z_{jet} and v_{jet} :

$$z_{\text{jet}} = 1.25(2r_c)^{1/2} (q_{\infty}\tau)^{1/4} \quad \text{and} \quad v_{\text{jet}} = 0.625 q_{\infty} (2r_c)^{1/2} (q_{\infty}\tau)^{-3/4}, \quad (22)$$

where we have made use of the value of the integral given in Table I corresponding to $n = 4$.

In order to deduce the equation for $r_{\text{jet}}(\tau)$, notice first that the sink distribution along the axis of symmetry $q_{\infty}(1 + |\Delta q|)$, with Δq the function represented in Fig. 8, exactly balances the flow rate imposed as the far-field boundary condition in Eq. (6). However, as shown in Fig. 9(a), the interface is a streamline in a frame of reference moving vertically with the velocity $dz_{\text{jet}}/d\tau$ along a distance $\sim r_{\text{jet}}$ extending upwards from the base of the jet, a fact meaning that the normal velocities to the interface in the moving frame of reference are zero in this region. Therefore, mass conservation enforces the emergence of a jet of width $\sim r_{\text{jet}}$ in order to compensate the flow rate which cannot be suctioned by the sink distribution $q_{\infty}(1 + |\Delta q|)$ where the normal velocities are zero in the moving frame of reference. Consequently, mass conservation demands that the flow rate which cannot be suctioned by the interface through this region of length $\sim r_{\text{jet}}$ is expelled into the gaseous atmosphere in the form of a jet of width r_{jet} given by:

$$2\pi \int_{z_{\text{jet}}}^{z_{\text{jet}}+r_{\text{jet}}} q_{\infty}[1 + |\Delta q(z)|] dz \approx 2\pi r_{\text{jet}}^2 \frac{dz_{\text{jet}}}{d\tau} \Rightarrow r_{\text{jet}} \frac{dz_{\text{jet}}}{d\tau} \simeq 1.7q_{\infty}, \quad (23)$$

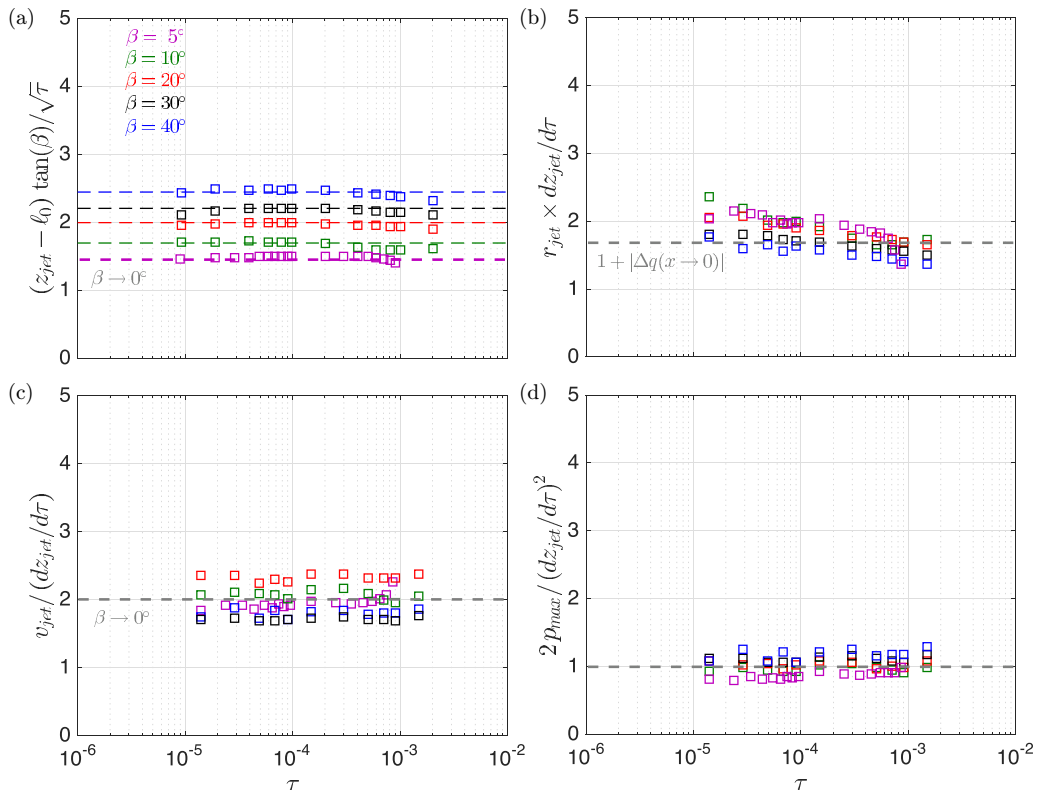


FIG. 10. Comparison between the numerical results in Appendix A corresponding to the case of conical cavities with different values of the opening semiangle β with the predictions in Eqs. (16), (23), and (25). Here $v_{\text{jet}}(\tau) = v_z[z = z_{\text{jet}}(\tau) + \alpha r_{\text{jet}}(\tau)]$ with $\alpha = 1$ for the case of slender cavities, namely the conical cavities with $\beta = 5^\circ$, $\beta = 10^\circ$, and $\beta = 20^\circ$, whereas $\alpha = 0$ for the cases of nonslender conical cavities, namely those with $\beta = 30^\circ$ and $\beta = 40^\circ$. The reason for the different values of α is that the liquid pressure relaxes to that of the gas at a different vertical locations within the jet depending on the value of the opening semiangle; see Fig. 9(c) for the case $\beta = 20^\circ$. Here $\ell_0(\beta = 5^\circ) = 0.0080$, $\ell_0(\beta = 10^\circ) = 0.0045$, $\ell_0(\beta = 20^\circ) = 0.0028$, $\ell_0(\beta = 30^\circ) = 0.0022$, and $\ell_0(\beta = 40^\circ) = 0.0012$.

where we have taken into account that (i) the rate of volume increase in the bulk of the liquid is $\pi r_{\text{jet}}^2 dz_{\text{jet}}/d\tau$; (ii) by virtue of the Euler-Bernoulli equation, the jet velocity in the moving frame of reference is $dz_{\text{jet}}/d\tau$; and (iii) the function Δq , represented in Fig. 10 is such that $-\Delta q(\bar{x} \rightarrow 0) \rightarrow 0.7$ and, consequently,

$$\int_{z_{\text{jet}}}^{z_{\text{jet}} + r_{\text{jet}}} |\Delta q| dz \simeq |\Delta q(\bar{x} = 0)| r_{\text{jet}} \approx 0.7 r_{\text{jet}}. \quad (24)$$

In order to validate the results in Eqs. (15), (16), (19), and (23) we make use of the results of the incompressible numerical simulations described in Appendix A. Indeed, in Appendix A we analyze the results of numerical simulations using the GERRIS [20,21] script used in Ref. [28] to simulate the emergence of very fast jets, with velocities up to 1000 m s^{-1} , which are emitted when a bubble cavitates in very close proximity to a solid wall once the value of the flow rate per unit length is prescribed as a far-field boundary condition. At this point, notice that our own analysis of the governing equations and of the numerical results reported in Appendix A permits us to conclude that both the jet shapes and the velocity field converge towards a β -dependent self-similar solution of the

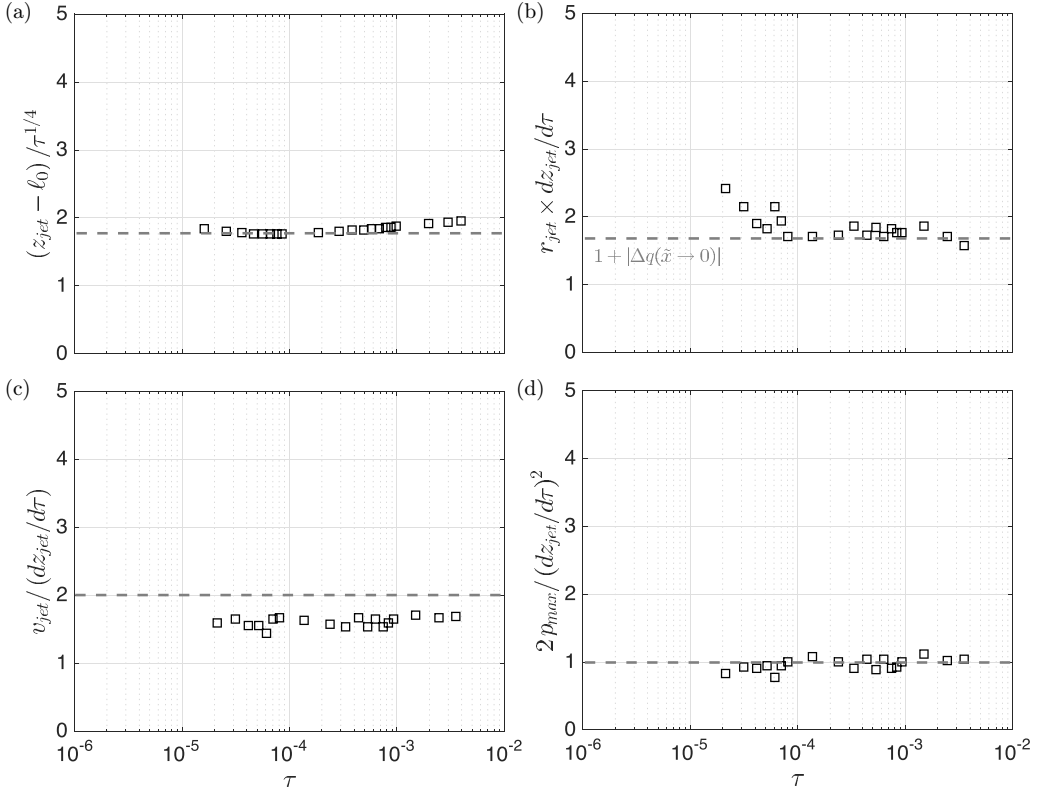


FIG. 11. Comparison between the numerical results of $p_{\max}(\tau) - p_{\text{gas}}$, $z_{\text{jet}}(\tau)$, $v_{\text{jet}}(\tau) = v_z(r=0, z = z_{\text{jet}} + r_{\text{jet}})$, and $r_{\text{jet}}(\tau)$ and the respective values predicted by Eqs. (16), (22), and (23). The reason for the small deviation between the predicted and the calculated jet velocity is because the liquid pressure relaxes to that of the gas at a vertical position within the jet which is slightly above $z = z_{\text{jet}}(\tau) + r_{\text{jet}}(\tau)$. Here $\ell_0(r_c = 1) = 0.015$.

Euler-Bernoulli and Laplace equations such that lengths and velocities are respectively proportional to $\sqrt{q_\infty \tau}$ and $\sqrt{q_\infty / \tau}$ for arbitrary values of β a result which, to our knowledge, had not been reported before.

Figure 10 compares the predictions given in Eqs. (16), (20), (21), and (23) with the numerical values of $r_{\text{jet}}(\tau)$, $v_{\text{jet}}(\tau)$, $p_{\max}(\tau)$, and of $r_{\text{jet}} dz_{\text{jet}} / d\tau(\tau)$ obtained from the numerical simulations detailed in Appendix A for the case of conical cavities with different values of the opening semiangle β taking $q_\infty = 1$. The results depicted in Fig. 10 confirm our predictions in the slender limit $\beta \ll 1$ and permit us to extend our results to generic values of β by just writing

$$z_{\text{jet}}(\beta, \tau) = K(\beta) z_{\text{jet}}(\beta \ll 1, \tau) = K(\beta) \frac{1.5}{\tan \beta} \sqrt{q_\infty \tau} \quad \text{with} \quad K(\beta \leq 5^\circ) = 1 \quad \text{and} \quad (25)$$

$K(\beta = 10^\circ) = 1.13$, $K(\beta = 20^\circ) = 1.33$, $K(\beta = 30^\circ) = 1.47$, and $K(\beta = 40^\circ) = 1.63$.

Moreover, Fig. 11 compares the predictions in Eqs. (16), (22), and (23) with the numerical values of $r_{\text{jet}}(\tau)$, $v_{\text{jet}}(\tau)$, $p_{\max}(\tau)$, and $r_{\text{jet}} dz_{\text{jet}} / d\tau(\tau)$ calculated using the same type of simulations as those detailed in Appendix A but replacing the equation for the initial shape of the interface by a parabola of equation $r_s(z, \tau = 0) = z^2/2$. The results shown in Fig. 11, which do not include any type of adjustable constant, provide further support to our theory.

In order to compare our predictions with the numerical results corresponding to the case of bubble bursting jets, we make use of the equations for r_{jet} and v_{jet} corresponding to the case of

conical cavities; see Eqs. (18), (23), and (25):

$$v_{\text{jet}} = \frac{1.5K(\beta)}{\tan \beta} \sqrt{\frac{q_\infty(r_{\text{jet}})}{\tau}}, \quad r_{\text{jet}} v_{\text{jet}} \simeq 3.4 q_\infty. \quad (26)$$

with $K(\beta \approx 40^\circ) \approx 1.6$; see Fig. 2(b). The results in Figs. 12(a) and 12(b) reveal that the predictions of Eqs. (26) for $We_l(\tau)$, $r_{\text{jet}}(\tau)$, and $z_{\text{jet}}(\tau)$ closely follow the numerical results and that, in contrast, the analogous scalings deduced using the inertio-capillary ansatz [35,36], $r_{\text{jet}} \propto \tau^{2/3}$, $v_{\text{jet}} \propto \tau^{-1/3}$, and $r_{\text{jet}} dz_{\text{jet}}/d\tau \propto \tau^{1/3}$, clearly deviate from the data. The results in Fig. 12 have been obtained for the slowly varying values of the forcing flow rate per unit length q_∞ given by the following:

$$\text{If } r_{\text{jet}} \geq r_{\text{jet0}}^* = 0.05 : \quad q_\infty = 0.82$$

$$\text{If } r_{\text{jet}} < r_{\text{jet0}}^* = 0.05 : \quad q_\infty(r_{\text{jet}}) = \frac{-r_0 \dot{r}_0(0)}{[r_0/(2r_c)(0)]} \times \exp\left(-\sqrt{\left\{\ln\left[\frac{r_0(0)}{2r_c(0)}\right]\right\}^2 - \ln\left[\frac{r_{\text{jet}}}{r_0(0)}\right]^2}\right), \quad (27)$$

see Fig. 3 in the Supplemental Material [48], where we find that $r_0(0) = 0.2$, $r_0 \dot{r}_0(0) = -1.5$, and $r_0(0)/[2r_c(0)] = 0.16$ for the whole range of $La < 2500$ considered here. The reason for the different expressions of the far-field forcing q_∞ in Eq. (27) can be explained as follows: For $r_{\text{jet}} > r_{\text{jet0}}^* \simeq 0.05$, the radius of the jet is sufficiently large for the flow rate per unit length $q_\infty \approx 1$ driving the jet ejection process to be fixed by the radial flow induced during the initial capillary collapse process of the cavity. However, for the cases corresponding to $La < 2500$, $r_{\text{jet}}(\tau \ll 1) \ll 1$ and, in addition, in these cases a tiny satellite bubble is entrapped beneath the bursting bubble. The satellite bubbles depicted in Fig. 3 (see also Fig. 1 in the Supplemental Material [48]) are produced as a result of the purely inertial collapse of a cylindrical gas thread and, consequently, when $r_{\text{jet}} \lesssim 0.05$, the flow rate per unit length $q_\infty < 0.82$ forcing the ejection of the jet is fixed by the value of the *local* flow rate per unit length driving the purely inertial pinch-off of the bubble at the instant when the collapsing bubble radius coincides with that of the jet. Hence, the result in Eq. (27) for the case $r_{\text{jet}} < 0.05$, which has been deduced making use of the theory in Ref. [17], simply reflects the well-known fact that the flow rate driving the pinch-off of bubbles [18,58–62], see also the Supplemental Material [48] for details, is a decreasing function of the minimum radius of the entrapped bubble.

Next we deduce the initial values of the jet width and velocity, namely the minimum value of the jet radius and the maximum value of the jet velocity for a given value of La . For $La \geq 2500$, the initial jet radius, r_{jet0} , is given by Eq. (1) and, from Eq. (26),

$$r_{\text{jet0}}(La > 2500) = 0.2215 \left(1 - \sqrt{\frac{\text{Oh}}{0.0305}}\right), \quad v_{\text{jet0}}(La > 2500) \simeq \frac{2.5}{r_{\text{jet0}}(La > 2500)}. \quad (28)$$

For the cases in which a bubble is entrapped, namely $La < 2500$, a jet will be ejected following the solution of Eqs. (26) and (27) if viscous effects are negligible, namely if the local Reynolds number $Re_l = \text{Oh}^{-1} r_{\text{jet}} v_{\text{jet}} \gtrsim O(1) \Rightarrow q_\infty \geq K \text{Oh}$ [32], with K a constant. Therefore, using the result in Eq. (27), the equations for the initial jet width and velocity deduced taking $q_\infty = K \text{Oh}$ when a bubble is entrapped, read:

$$r_{\text{jet0}}(La < 2500) = r_0(0) \times \exp\left[-\frac{1}{2} \left(\left\{ \ln\left[\frac{-K\text{Oh} r_0(0)}{(2r_c r_0 \dot{r}_0)(0)}\right] \right\}^2 - \left\{ \ln\left[\frac{r_0(0)}{2r_c(0)}\right] \right\}^2 \right)\right]$$

$$v_{\text{jet0}}(La < 2500) = \frac{3.4 q_\infty(r_{\text{jet0}})}{r_{\text{jet0}}} = \frac{3.4 K \text{Oh}}{r_{\text{jet0}}(La < 2500)}, \quad (29)$$

where we have made use of the second of the equations in (26). The predictions in Eqs. (29) taking $K = 10$ are pretty close to the numerical values depicted in Figs. 12(c) and 12(d).

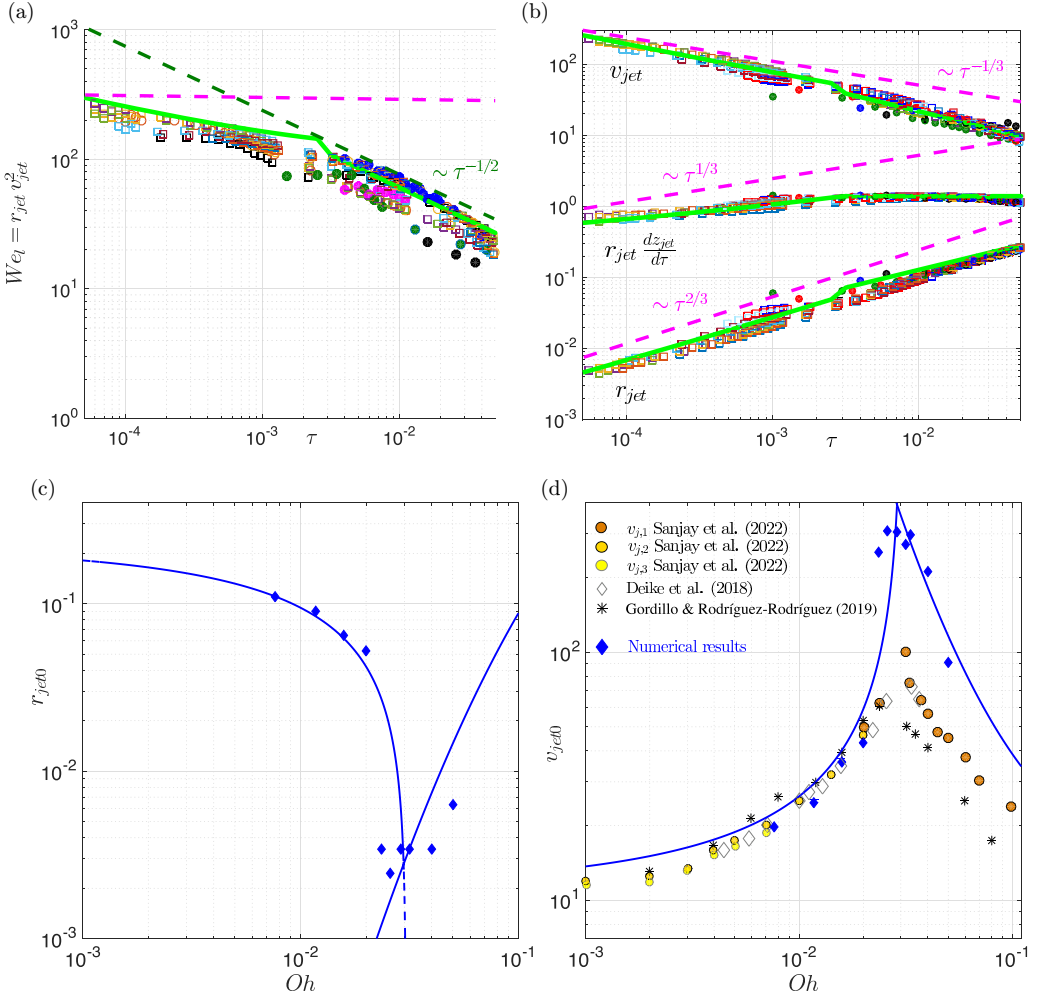


FIG. 12. (a) $We_l = r_{\text{jet}} v_{\text{jet}}^2 \gg 1$, with $We_l \propto \tau^{-1/2}$ for $\tau \gtrsim 10^{-3}$. The green line indicates the predicted values of $We_l[r_{\text{jet}}(\tau)] = v_{\text{jet}}^2 r_{\text{jet}} = \{3.4 q_\infty [r_{\text{jet}}(\tau)]^2 / r_{\text{jet}}(\tau)\}$, with r_{jet} and v_{jet} calculated using Eqs. (26) and (27). (b) The values of $v_{\text{jet}}(\tau)$, $r_{\text{jet}} dz_{\text{jet}}/d\tau$, and $r_{\text{jet}}(\tau)$ calculated using Eqs. (26) and (27), in green, reproduce the numerical results. In contrast, the inertio-capillary predictions [35,36], in pink, $v_{\text{jet}} \propto \tau^{-1/3}$, $r_{\text{jet}} dz_{\text{jet}}/d\tau \propto \tau^{1/3}$, and $r_{\text{jet}} \propto \tau^{2/3}$, substantially deviate from the data. The numerical values in the figure correspond to $\tau > \tau^*(La)$, with $\tau^*(La) > 0$ the instant of time such that $(z_{\text{tip}} - z_{\text{jet}})/r_{\text{jet}} \geq 1.25$; see Fig. 1 and Fig. 2 in SM. [(c) and (d)] Comparison of the numerical values of $r_{\text{jet}0}(La)$ and $v_{\text{jet}0}(La)$ with the predictions (blue continuous line) in Eqs. (28) and (29). The numerical results in Ref. [57] for $v_{\text{jet}0}$ are also included in Fig. 12(d). The differences existing between their results and ours for $La < 2500$ are attributable to the differences existing in the instant of time at which the numerical values are calculated: In our case, the numerical values corresponds to instants of time $\tau \sim 10^{-5}$. Notice that the diameter and the velocity of the first drop ejected can be calculated using the ballistic equations in Refs. [15,49] using the results in this figure. Notice, however, that, as was pointed out in Ref. [12], for $La \gtrsim 2500$, the tip of the jet is hardly decelerated by capillary forces and by the viscous drag exerted by the gas, a fact implying that Eqs. (28) can be used to approximate the diameter and the initial velocity of the first drop ejected.

As pointed out in Sec. II, the values of $r_{\text{jet0}}(\text{La})$ and $v_{\text{jet0}}(\text{La})$ deduced above when a bubble is entrapped are not the ones of the initial drop radius and velocity which, however, can be expressed as a function of $r_{\text{jet}}(\tau)$ and of $v_{\text{jet}}(\tau)$ following the results in Ref. [49], where the ballistic equations deduced in Ref. [15] are coupled with the mass and the momentum balances at the top drop [63].

As a final remark, notice that both the numerical simulations and the theoretical results have been deduced under the incompressible approximation and under the assumption that both the cavity collapse process and the jet produced, are axisymmetric. In real applications, however, asymmetries are always present but Ref. [64] showed that the amplitude of these asymmetries does not grow during the cavity collapse process. Then, when the minimum radius of the cavity equals the amplitude of the asymmetry, the liquid is no longer accelerated inwards, the cavity breaks and a jet is issued [15]. This fact possesses two important implications for the dynamics of the jet: On the one hand, the ejected jet is not axisymmetric, as it can be clearly appreciated in the experiments reported in Ref. [15] and in the experiments with cavitation bubbles reported in Ref. [28] and, on the other hand, provided that the local Reynolds number at the instant of jet ejection is large, the equation expressing that the minimum radius of the imploding cavity equals the amplitude of the asymmetry, sets the value of the minimum jet radius r_{jet0} and also the maximum value for the jet velocity, v_{jet0} , through the mass conservation equation derived above, $r_{\text{jet0}} v_{\text{jet0}} \simeq 3.4 q_{\infty}$; see Eq. (23). Consequently, the viscous cut-off values of $r_{\text{jet0}}(\text{La})$ and $v_{\text{jet0}}(\text{La})$ deduced here will describe a real experiment provided that the amplitude of the asymmetries is smaller than $r_{\text{jet0}}(\text{La})$.

IV. CONCLUSIONS

To conclude, here we have analyzed the high-Reynolds number implosion of cavities under the incompressible approach when the collapse is driven by a far-field boundary condition expressing that the flow rate per unit length remains constant in time. We have presented a self-consistent theory which describes the collapse of slender axisymmetric cavities with a generic geometry and provides with algebraic equations, with no adjustable constants, for the time evolution of the speed, width, and of the vertical position of the jets. When particularized to the case of conical bubbles, our algebraic equations reproduce the self-similar results obtained numerically in the limit of small values of the opening semiangle and, when particularized to the case of parabolic cavities, we also find that our predictions for the jet radius, the jet velocity, and the maximum liquid pressure are in good agreement with simulations. We have also shown here that the jets produced right after a bubble bursts at an interface can be described in terms of our purely inertial theory, which differs from the common belief that the dynamics of the jets produced after the inertio-capillary collapse of cavities can be described in terms of an inertio-capillary balance; see, e.g., Ref. [36]. For the case of bubble bursting jets, we have also deduced the equations describing the time-varying jet radius $r_{\text{jet}}(\tau, \text{La}) \geq r_{\text{jet0}}(\text{La})$ and the velocity $v_{\text{jet}}(\tau, \text{La}) \leq v_{\text{jet0}}(\text{La})$, as well as the initial values of the jet radius and of the jet velocity, i.e., $r_{\text{jet0}}(\text{La})$ and $v_{\text{jet0}}(\text{La})$, respectively. Our predictions agree well with the numerical results, which could reproduce a real experiment provided that the amplitude of the unavoidable asymmetries do not disturb the interface before the jet is ejected. As shown in Ref. [49], the time-dependent jet shape and the time-dependent velocity field within the jet can be expressed in closed form in terms of the time-dependent functions $r_{\text{jet}}(\text{La}, \tau)$, $z_{\text{jet}}(\text{La}, \tau)$, and $v_{\text{jet}}(\text{La}, \tau)$, which constitute the initial conditions of the ballistic equations deduced in Ref. [15]. Hence, here we provide with the necessary information for the correct quantification of the different fluxes transported by bubble bursting jets from the ocean into the atmosphere. In spite of the results presented here resort on the incompressible approximation, they might also be applied to describe the type of very high speed jets generated when a conical bubble implodes very close to a wall, a phenomenon which could play a role in the degradation of the material produced by liquid cavitation.

ACKNOWLEDGMENTS

This research work has been partially supported by the Grant No. PID2020-115655GB-C21 financed by the Spanish MCIN/ AEI/10.13039/501100011033. J.M.G. designed the research and the theory, analyzed the data, and wrote the paper, and F.J.B.-R. performed the numerical simulations and analyzed the data. All authors reviewed the results and approved the final version of the paper.

APPENDIX A: SELF-SIMILAR CONICAL JETS

In this Appendix we present numerical results describing the high-Reynolds-number implosion of conical voids such as those found in the collapsing depressions of standing waves [35], during the collapse of bursting bubbles [29,32], or as a consequence of the collapse of the cavity formed after a drop impacts a liquid pool [9,10,12]. The numerical results have been obtained using the open-source package GERRIS [20,21] and therefore the effects of compressibility on the collapse and jet ejection processes are not retained in the simulations. In fact, the results in this section have been obtained using the GERRIS script provided in Ref. [28] in their study of the dynamic of jets produced in cavitation bubbles near a rigid boundary for small values of the standoff parameter. The numerical setup in Fig. 13(a) illustrates the radial and axial coordinates, R and Z , respectively; the initial shape of a conical cavity with a half-opening angle β ; and L_c , namely the radius of the cylindrical surface where the value of the far-field radial velocity, V_c , is imposed. In the following, ρ , μ , and σ will respectively denote the liquid density, viscosity, and interfacial tension coefficient, whereas ρ_g and μ_g will be used to refer to the gas density and viscosity. The numerical code is solved fixing the value of the flow rate per unit length, $L_c V_c$, at $R = L_c$ and imposing outflow boundary conditions at $Z = \pm L_c/2$, i.e., the Z derivatives of the velocity and pressure fields are zero at the top and bottom boundaries. The minimum grid size is $2^{-12} L_c$ and the jet radius at the region where it meets the conical surface [see Fig. 13(b)] will be resolved with at least six numerical cells.

Using L_c , L_c/V_c , and ρV_c^2 as the characteristic scales of length, time, and pressure, the flow sketched in Fig. 13(a) can be described in terms of the following dimensionless parameters:

$$\text{We} = \frac{\rho V_c^2 L_c}{\sigma}, \quad \text{Re} = \frac{\rho V_c L_c}{\mu}, \quad m = \frac{\mu_g}{\mu}, \quad \Lambda = \frac{\rho_g}{\rho}, \quad \text{and} \quad \beta, \quad (\text{A1})$$

but, since here we fix the values of the density and viscosity ratios to those characterizing the air-water system, $\Lambda = 1.2 \times 10^{-3}$, $m = 1.8 \times 10^{-2}$, the numerical solutions will only depend on We , Re , and β . Notice also that, from now on, dimensionless variables will be written using lowercase letters to differentiate them from their dimensional counterparts, written in capitals, and τ and \mathbf{n} will indicate, respectively, the dimensionless time after the jet is ejected and the unit normal vector to the interface of equation

$$r = r_s(z, \tau) \Rightarrow F = r - r_s(z, \tau) = 0. \quad (\text{A2})$$

Figure 14 shows that the numerical results are virtually independent of both We and Re for the range of values of these two parameters considered in this study, namely $\text{Re} \geq 50$ and $\text{We} \geq 0.5$. While the results regarding the effect of the Reynolds number could have been anticipated in view of the fact that the minimum value of Re is already large, $\text{Re} = 50$, the independence of the solution with We indicates that the mechanism of jet ejection is not driven by capillarity. The influence of the opening semiangle β on the temporal evolution of the jet shapes is analyzed in Fig. 15, where it can be clearly appreciated that the jet velocity increases when β decreases.

It is our purpose now to explore whether there exists a self-similar solution for the high-Reynolds number jets depicted in Fig. 15 for instants of time such that $\tau \ll 1$. The analysis starts by considering that the vorticity production at the interface can be neglected in the description of the jet dynamics in the limit $\text{Re} \gg 1$ and then the velocity field \mathbf{v} can be expressed in terms of the velocity

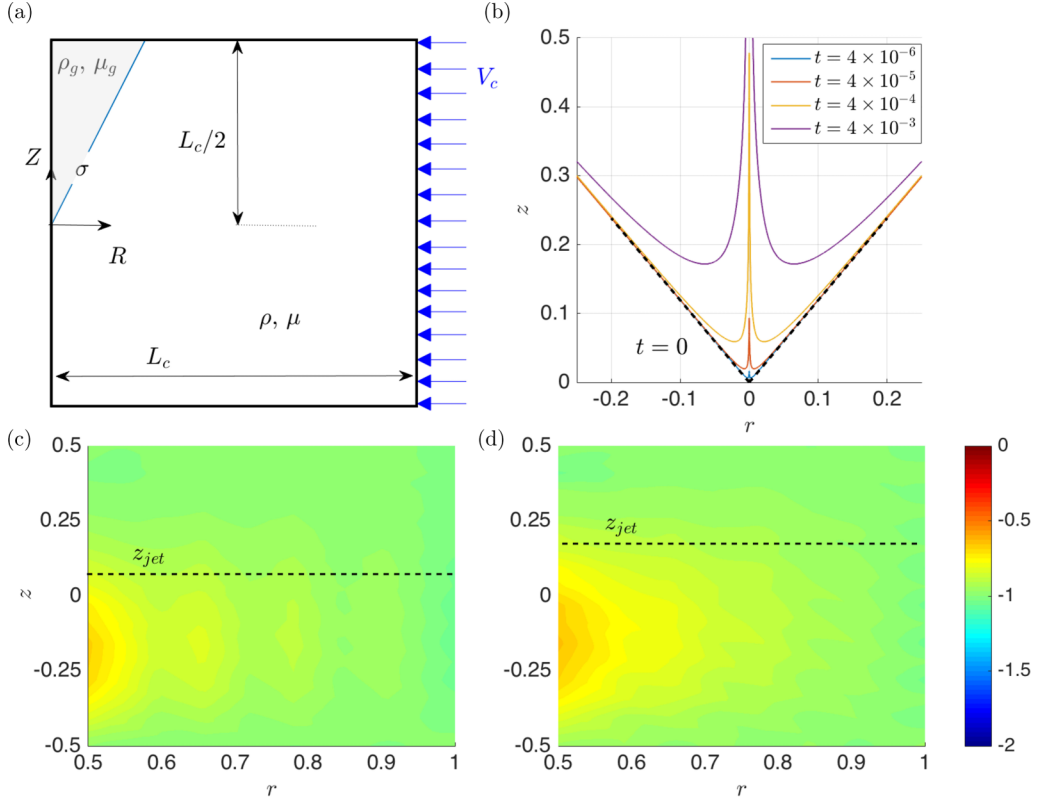


FIG. 13. (a) Sketch of the numerical setup indicating the far-field boundary condition, the initial shape of the conical interface, the material properties of the liquid and the gas, as well as the radial and axial coordinates, R and Z , respectively. (b) Numerical results corresponding to $\text{Re} = 100$, $\text{We} = 1$, and $\beta = 40^\circ$. [(c) and (d)] Numerical values of rv_r corresponding to the simulations depicted in (b) at two different instants of time: $\tau = 4 \times 10^{-4}$ (c) and $\tau = 4 \times 10^{-3}$ (d). Notice that the type of numerical simulations carried out using the boundary conditions sketched in (a) impose, as a far-field boundary condition, a constant value of the flow rate per unit length, $rv_r \rightarrow -1$.

potential ϕ as

$$\mathbf{v} = \nabla\phi. \quad (\text{A3})$$

Therefore, in the incompressible limit of interest here, continuity demands that

$$\nabla \cdot \mathbf{v} = 0 \Rightarrow \nabla^2\phi = 0, \quad (\text{A4})$$

where we have made use of Eq. (A3). The Laplace equation (A4) must be solved subjected to the value of the velocity potential calculated particularizing the Euler-Bernoulli equation

$$\frac{\partial\phi}{\partial\tau} + \frac{|\nabla\phi|^2}{2} - \text{We}^{-1} \nabla \cdot \mathbf{n} = C(\tau) \quad (\text{A5})$$

at the interface of equation $F = 0$, with F the function defined in (A2) satisfying the kinematic boundary condition,

$$\frac{DF}{Dt} = 0 \Rightarrow \frac{\partial\phi}{\partial r} = \frac{\partial r_s}{\partial\tau} + \frac{\partial\phi}{\partial z} \frac{\partial r_s}{\partial z}, \quad \text{with} \quad r_s(z \rightarrow \infty, \tau) \rightarrow z \tan\beta \quad (\text{A6})$$

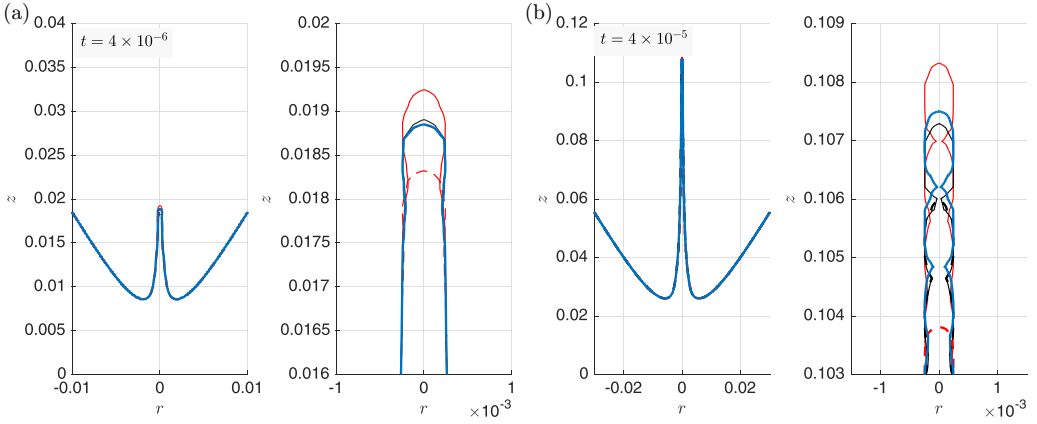


FIG. 14. Analysis of the influence of Re and We on the jet ejection process for a fixed value of $\beta = 30^\circ$ and two different instants of time $\tau = 4 \times 10^{-6}$ (a) and $\tau = 4 \times 10^{-5}$ (b). The results in the figure have been obtained for the following values of the control parameters: $Re = 100$ and $We = 1$ (blue continuous line); $Re = 50$ and $We = 1$ (red dashed line); $Re = 200$ and $We = 1$ (red continuous line); $Re = 100$ and $We = 5$ (black continuous line); and $Re = 100$ and $We = 0.5$ (black dashed line). Notice that the differences between the jet shapes are practically indistinguishable and are only appreciable in the zoomed images corresponding to the jet tip, a fact indicating that the spatiotemporal evolution of the jet is virtually independent of Re and We .

and with D/Dt indicating the material derivative. In Ref. [35], the self-similar structure of the flow field was deduced, introducing the scaled variables

$$\phi = (\tau - \tau_0)^\delta h \left[\frac{z - \ell_0}{(\tau - \tau_0)^\varepsilon}, \frac{r}{(\tau - \tau_0)^\varepsilon} \right] \quad \text{and} \quad r_s(z, \tau) = (\tau - \tau_0)^\varepsilon g \left[\frac{z - \ell_0}{(\tau - \tau_0)^\varepsilon} \right] \quad (\text{A7})$$

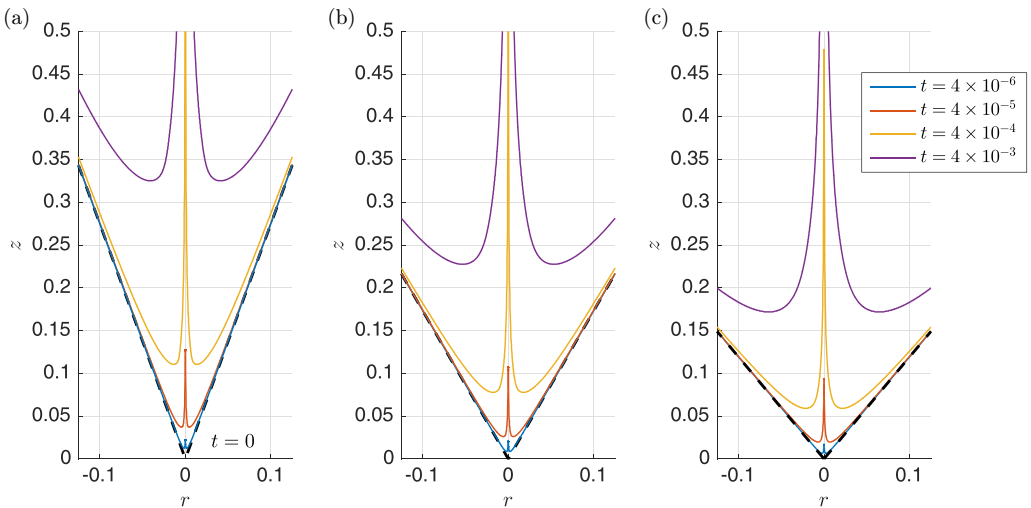


FIG. 15. This figure analyzes the influence of the opening semiangle on the spatiotemporal evolution of the jet: (a) $\beta = 20^\circ$, (b) $\beta = 30^\circ$, and (c) $\beta = 40^\circ$. In the three cases considered, $Re = 100$ and $We = 1$. Notice that the jet speed increases when β decreases.

into the system of Eqs. (A4)–(A6), finding that both Eqs. (A4) and (A6) can be written in terms of the self-similar variables defined in (A7) if $\delta = 2\varepsilon - 1$, with this condition also ensuring that the terms $\partial\phi/\partial\tau$ and $|\nabla\phi|^2/2$ in the Euler-Bernoulli equation (A5) possess an identical functional dependence with time. In Ref. [35], the value of the exponent $\varepsilon = 2/3$ characterizing the length scale in their inertio-capillary self-similar solutions was deduced imposing the additional condition that the time dependence of the three terms at the left-hand side of Eq. (A5) must be the same.

However, the results depicted in Fig. 14 reveal that the time evolution of the jet is independent of the Weber number, a fact indicating that the type of jets considered here are not forced by capillarity. Consequently, in the present case, the only restriction imposed by Eqs. (A4)–(A6) for self-similar solutions to exist is that $\delta = 2\varepsilon - 1$ and then the value of the exponent ε in Eq. (A7) should be fixed by the far-field boundary condition of the Laplace equation (A4) which, in our case, reads; see Fig. 13:

$$r \frac{\partial\phi}{\partial r} \rightarrow -1 \quad \text{for } r \rightarrow \infty. \quad (\text{A8})$$

The far-field boundary condition (A8) differs from the one corresponding to the inertio-capillary collapse of a cavity, which happens to be analogous to that driving the self-similar wave created after the impact of a disk over a liquid pool. Indeed, in this latter case, Refs. [65,66] reported that the far-field boundary condition for the velocity potential is the well-known two-dimensional irrotational flow around a wedge of angle 2π ,

$$\phi(r \rightarrow \infty) \propto r^{1/2} w(\theta), \quad (\text{A9})$$

with r and θ indicating the polar coordinates. The different boundary conditions (A8) and (A9) explain the differences between the exponent $\varepsilon = 2/3$ characterizing the self-similar solutions reported in Refs. [35,66] and the corresponding value of ε which is imposed by Eq. (A8). Indeed, here $\varepsilon = 1/2$ because, as pointed out above, $\delta = 2\varepsilon - 1$ and, in addition, Eq. (A8) can only be written in terms of the self-similar variables defined in (A7) if $\delta = 0$. Since $\varepsilon = 1/2$, in the case the numerical solution converged to a self-similar solution of the system of equations and boundary conditions for sufficiently large values of $\tau > \tau_0$, the characteristic length scale of the jets depicted in Fig. 14 should depend on time as $(\tau - \tau_0)^{1/2}$, whereas velocities should depend on time as $(\tau - \tau_0)^{-1/2}$, with these predictions also implying that, in the limit $(\tau - \tau_0) \ll 1$ of interest here, both C and the capillary term in Eq. (A5) are subdominant with respect to the inertial terms $\partial\phi/\partial\tau$ and $|\nabla\phi|^2/2$.

In view of the previous analysis, here explore whether the different jet shapes depicted in Fig. 15 can be collapsed onto a single curve. For this purpose, we define the time-dependent functions $z_{\text{jet}}(\tau, \beta)$ and $r_{\text{jet}}(\tau, \beta)$ illustrated in Fig. 6. Figure 16 shows that the time-dependent jet shapes depicted in Fig. 15 do indeed collapse for over two decades in time onto a time-independent and almost β -independent function when plotted in terms of the scaled radial and vertical coordinates suggested by our previous analysis and defined as

$$\chi = \frac{r}{r_{\text{jet}}(\tau, \beta)}, \quad \text{and} \quad \eta = \frac{z - \ell_0(\beta)}{z_{\text{jet}}(\tau, \beta) - \ell_0(\beta)}, \quad (\text{A10})$$

with the values of $\ell_0(\beta)$ given in Fig. 10, where it is depicted that, indeed, $z_{\text{jet}}(\tau, \beta) - \ell_0(\beta) \propto \tau^{1/2}$, $d z_{\text{jet}}/d\tau \propto \tau^{-1/2}$, and $r_{\text{jet}}(\tau, \beta) \propto \tau^{1/2}$.

The numerical results corresponding the case of a parabolic cavity shown in Fig. 11, have been obtained using the same numerical code and the same boundary conditions as those detailed in this Appendix, being the only difference that the equation for the initial shape of the interface is, in this case, $r_s(z, \tau = 0) = z^2/2$.

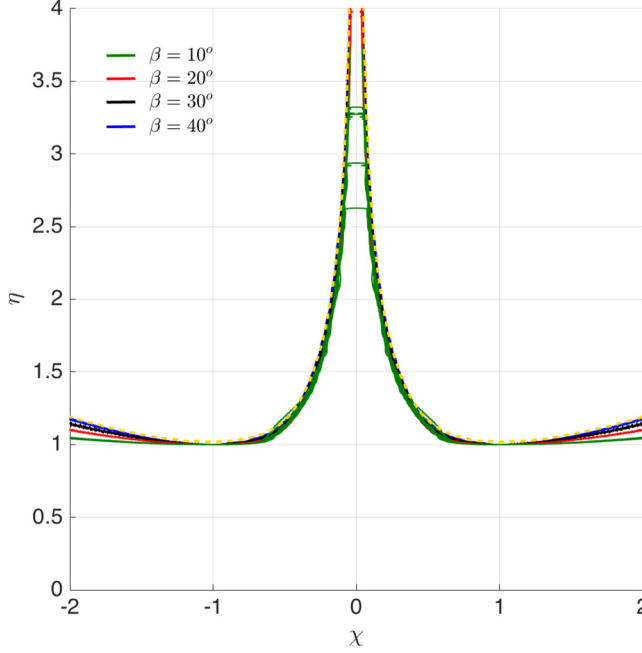


FIG. 16. The spatiotemporal evolution of the jet shapes of the type shown in Fig. 15 collapse, along two decades in time and for four different values of β , namely $\beta = 10^\circ$, 20° , 30° , and 40° , onto the τ -independent and almost β -independent function depicted in the figure, with χ and η defined in Eq. (A10). This function for the self-similar shapes of the jets is compared in Fig. 5 with the numerical results obtained for the case of bubble bursting jets emerging from the base of a truncated conical surface.

APPENDIX B: SOLUTION OF THE INTEGRAL EQUATION FOR Δq

Equation (11) is solved integrating by parts, once we notice that the integrands in Eq. (11) can be written, for $\bar{z} > \bar{z}_0$, as:

$$\frac{df/d\bar{z}_0}{(\bar{z} - \bar{z}_0)^2} = \frac{d}{d\bar{z}_0} \left[\frac{f}{(\bar{z} - \bar{z}_0)^2} \right] - 2 \frac{f}{(\bar{z} - \bar{z}_0)^3} \quad (\text{B1})$$

and for $\bar{z} < \bar{z}_0$ as:

$$-\frac{df/d\bar{z}_0}{(\bar{z} - \bar{z}_0)^2} = - \left\{ \frac{d}{d\bar{z}_0} \left[\frac{f}{(\bar{z} - \bar{z}_0)^2} \right] - 2 \frac{f}{(\bar{z} - \bar{z}_0)^3} \right\}. \quad (\text{B2})$$

Notice that

$$\lim_{\gamma \rightarrow 0} \int_1^{\bar{z}-\gamma} \frac{d}{d\bar{z}_0} \left[\frac{f}{(\bar{z} - \bar{z}_0)^2} \right] d\bar{z}_0 = \frac{f(\bar{z})}{\gamma^2}, \quad (\text{B3})$$

where we have taken into account that $f(\bar{z} = 1) = 0$. Moreover, notice that

$$\lim_{\gamma \rightarrow 0} \int_{\bar{z}+\gamma}^{\infty} - \frac{d}{d\bar{z}_0} \left[\frac{f}{(\bar{z} - \bar{z}_0)^2} \right] d\bar{z}_0 = \frac{f(\bar{z})}{\gamma^2}. \quad (\text{B4})$$

We now discretize f , which is assumed to be constant and of value $f(\bar{z}_i) = f_i$ along N panels of constant width h , centered at $\bar{z}_i = 1 + 3h/4 + (i-1)h$. Then, for $i > j$:

$$\int_{\bar{z}_j-h/2}^{\bar{z}_j+h/2} - \frac{2f_j}{(\bar{z}_i - \bar{z}_0)^3} d\bar{z}_0 = -f_j \left[\frac{1}{(\bar{z}_i - \bar{z}_j - h/2)^2} - \frac{1}{(\bar{z}_i - \bar{z}_j + h/2)^2} \right], \quad (\text{B5})$$

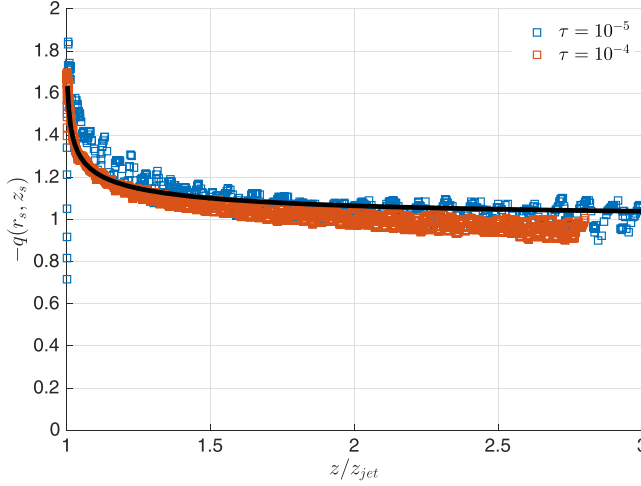


FIG. 17. The numerical values of $-q(r_s, v_s) = -r_s(z, \tau)v_r(r = r_s, z, \tau)$ calculated at two instants of time for a value of the opening semiangle $\beta = 5^\circ$ are compared with $q_\infty(1 + |\Delta q|)$ (black continuous line) with Δq given in Fig. 8, finding good agreement between simulations and the theoretical prediction.

for $i < j$:

$$\int_{\bar{z}_j - h/2}^{\bar{z}_j + h/2} \frac{2f_j}{(\bar{z}_i - \bar{z}_0)^3} d\bar{z}_0 = f_j \left[\frac{1}{(\bar{z}_i - \bar{z}_j - h/2)^2} - \frac{1}{(\bar{z}_i - \bar{z}_j + h/2)^2} \right], \quad (\text{B6})$$

whereas for $i = j$:

$$\begin{aligned} \int_{\bar{z}_i - h/2}^{\bar{z}_i - \gamma} \frac{2f_i}{(\bar{z}_i - \bar{z}_0)^3} d\bar{z}_0 &= -f_i \left[\frac{1}{\gamma^2} - \frac{1}{(h/2)^2} \right] \quad \text{and} \\ \int_{\bar{z}_i + \gamma}^{\bar{z}_i + h/2} \frac{2f_i}{(\bar{z}_i - \bar{z}_0)^3} d\bar{z}_0 &= f_i \left[-\frac{1}{\gamma^2} + \frac{1}{(h/2)^2} \right] \end{aligned} \quad (\text{B7})$$

For values $\bar{z} > \bar{z}_N + h/2$, with $\bar{z}_N \gg 1$ we impose mass conservation, namely that the flow rate injected by the distribution of sources located at $0 \leq \bar{z} \leq 1$ equals the flow rate through the free interface; see Eq. (11):

$$\int_1^\infty \Delta q d\bar{z} = \int_1^\infty \frac{df}{d\bar{z}} d\bar{z} = f_\infty = -1 \quad (\text{B8})$$

and, therefore, the integral in Eq. (11) for $\bar{z} > \bar{z}_N + h/2$ can be solved analytically to give:

$$\int_{\bar{z}_N + h/2}^\infty \frac{2f_\infty}{(\bar{z}_i - \bar{z}_0)^3} d\bar{z}_0 = \frac{1}{(\bar{z}_i - \bar{z}_N - h/2)^2} \quad (\text{B9})$$

The numerical code provided in the Supplemental Material [48] solves the integral equation (11) using the results in Eqs. (B1)–(B9) and, once the function f is calculated solving the resulting linear system of equations, the function Δq is calculated as

$$\Delta q_i = \Delta q(\bar{z}_i) = \frac{f_{i+1} - f_i}{h}. \quad (\text{B10})$$

The results in Fig. 17 compare the values of the flow rate at the interface calculated numerically as $-q(r_s, v_s) = -r_s(z, \tau)v_r(r = r_s, z, \tau)$ for a value of the opening semiangle $\beta = 5^\circ$ with our

prediction, $q_\infty(1 + |\Delta q|)$, at two different instants of time, finding good agreement between our theory and the numerical results.

-
- [1] C.-D. Ohl, M. Arora, R. Dijkink, V. Janve, and D. Lohse, Surface cleaning from laser-induced cavitation bubbles, *Appl. Phys. Lett.* **89**, 074102 (2006).
 - [2] C. Lechner, W. Lauterborn, M. Koch, and R. Mettin, Fast, thin jets from bubbles expanding and collapsing in extreme vicinity to a solid boundary: A numerical study, *Phys. Rev. Fluids* **4**, 021601(R) (2019).
 - [3] P. L. L. Walls, J. C. Bird, and L. Bourouiba, Moving with bubbles: A review of the interactions between bubbles and the microorganisms that surround them, *Integr. Comp. Biol.* **54**, 1014 (2014).
 - [4] L. Dubitsky, O. McRae, and J. C. Bird, Enrichment of Scavenged Particles in Jet Drops Determined by Bubble Size and Particle Position, *Phys. Rev. Lett.* **130**, 054001 (2023).
 - [5] G. Birkhoff, D. P. MacDougall, E. M. Pugh, and S. G. Taylor, Explosives with lined cavities, *J. Appl. Phys.* **19**, 563 (1948).
 - [6] Y. Tagawa, N. Oudalov, C. W. Visser, I. R. Peters, D. van der Meer, C. Sun, A. Prosperetti, and D. Lohse, Highly Focused Supersonic Microjets, *Phys. Rev. X* **2**, 031002 (2012).
 - [7] I. R. Peters, Y. Tagawa, N. Oudalov, C. Sun, A. Prosperetti, D. Lohse, and D. van der Meer, Highly focused supersonic microjets: Numerical simulations, *J. Fluid Mech.* **719**, 587 (2013).
 - [8] B. Ray, G. Biswas, and A. Sharma, Regimes during liquid drop impact on a liquid pool, *J. Fluid Mech.* **768**, 492 (2015).
 - [9] G.-J. Michon, C. Josserand, and T. Séon, Jet dynamics post drop impact on a deep pool, *Phys. Rev. Fluids* **2**, 023601 (2017).
 - [10] S. T. Thoroddsen, K. Takehara, H. D. Nguyen, and T. G. Etoh, Singular jets during the collapse of drop-impact craters, *J. Fluid Mech.* **848**, R3 (2018).
 - [11] Z. Q. Yang, Y. S. Tian, and S. T. Thoroddsen, Multitude of dimple shapes can produce singular jets during the collapse of immiscible drop-impact craters, *J. Fluid Mech.* **904**, A19 (2020).
 - [12] F. J. Blanco-Rodríguez and J. M. Gordillo, On the jets produced by drops impacting a deep liquid pool and by bursting bubbles, *J. Fluid Mech.* **916**, A37 (2021).
 - [13] Y. S. Tian, Z. Q. Yang, and S. T. Thoroddsen, Conical focusing: Mechanism for singular jetting from collapsing drop-impact craters, *J. Fluid Mech.* **958**, R1 (2023).
 - [14] S. Gekle, J. M. Gordillo, D. van der Meer, and D. Lohse, High-Speed Jet Formation After Solid Object Impact, *Phys. Rev. Lett.* **102**, 034502 (2009).
 - [15] S. Gekle and J. M. Gordillo, Generation and breakup of Worthington jets after cavity collapse. Part 1. Jet formation, *J. Fluid Mech.* **663**, 293 (2010).
 - [16] S. Krishnan, E. J. Hopfinger, and B. A. Puthenveetil, On the scaling of jetting from bubble collapse at a liquid surface, *J. Fluid Mech.* **822**, 791 (2017).
 - [17] J. M. Gordillo, Axisymmetric bubble collapse in a quiescent liquid pool. i. Theory and numerical simulations, *Phys. Fluids* **20**, 112103 (2008).
 - [18] R. Bolaños-Jiménez, A. Sevilla, C. Martínez-Bazán, and J. M. Gordillo, Axisymmetric bubble collapse in a quiescent liquid pool. ii. Experimental study, *Phys. Fluids* **20**, 112104 (2008).
 - [19] T. Séon and A. Antkowiak, Large Bubble Rupture Sparks Fast Liquid Jet, *Phys. Rev. Lett.* **109**, 014501 (2012).
 - [20] S. Popinet, Gerris: A tree-based adaptive solver for the incompressible Euler equations in complex geometries, *J. Comput. Phys.* **190**, 572 (2003).
 - [21] S. Popinet, An accurate adaptive solver for surface-tension-driven interfacial flows, *J. Comput. Phys.* **228**, 5838 (2009).
 - [22] A. Antkowiak, N. Bremond, S. Le Dizes, and E. Villermaux, Short-term dynamics of a density interface following an impact, *J. Fluid Mech.* **577**, 241 (2007).

- [23] J. M. Gordillo, H. Onuki, and Y. Tagawa, Impulsive generation of jets by flow focusing, *J. Fluid Mech.* **894**, A3 (2020).
- [24] H. Onuki, Y. Oi, and Y. Tagawa, Microjet Generator for Highly Viscous Fluids, *Phys. Rev. Appl.* **9**, 014035 (2018).
- [25] A. Fraters, M. Rump, R. Jeurissen, M. van den Berg, Y. de Loore, H. Reinten, H. Wijshoff, D. van der Meer, D. Lohse, M. Versluis, and T. Segers, Meniscus Oscillations Driven by Flow Focusing Lead to Bubble Pinch-Off and Entrainment in a Piezoacoustic Inkjet Nozzle, *Phys. Rev. Appl.* **16**, 044052 (2021).
- [26] J. R. Blake and D. C. Gibson, Cavitation bubbles near boundaries, *Annu. Rev. Fluid Mech.* **19**, 99 (1987).
- [27] O. Supponen, D. Obreschkow, M. Tinguely, P. Kobel, N. Dorsaz, and M. Farhat, Scaling laws for jets of single cavitation bubbles, *J. Fluid Mech.* **802**, 263 (2016).
- [28] F. Reuter and C.-D. Ohl, Supersonic needle-jet generation with single cavitation bubbles, *Appl. Phys. Lett.* **118**, 134103 (2021).
- [29] L. Duchemin, S. Popinet, C. Josserand, and S. Zaleski, Jet formation in bubbles bursting at a free surface, *Phys. Fluids* **14**, 3000 (2002).
- [30] L. Deike, E. Ghabache, G. Liger-Belair, A. K. Das, S. Zaleski, S. Popinet, and T. Seon, Dynamics of jets produced by bursting bubbles, *Phys. Rev. Fluids* **3**, 013603 (2018).
- [31] C. F. Brasz, C. T. Bartlett, P. L. L. Walls, E. G. Flynn, Y. E. Yu, and J. C. Bird, Minimum size for the top jet drop from a bursting bubble, *Phys. Rev. Fluids* **3**, 074001 (2018).
- [32] J. M. Gordillo and J. Rodríguez-Rodríguez, Capillary waves control the ejection of bubble bursting jets, *J. Fluid Mech.* **867**, 556 (2019).
- [33] A. Berny, L. Deike, T. Séon, and S. Popinet, Role of all jet drops in mass transfer from bursting bubbles, *Phys. Rev. Fluids* **5**, 033605 (2020).
- [34] E. Ghabache and T. Seon, Size of the top jet drop produced by bubble bursting, *Phys. Rev. Fluids* **1**, 051901(R) (2016).
- [35] B. W. Zeff, B. Kleber, J. Fineberg, and D. P. Lathrop, Singularity dynamics in curvature collapse and jet eruption on a fluid surface, *Nature* **403**, 401 (2000).
- [36] C.-Y. Lai, J. Eggers, and L. Deike, Bubble Bursting: Universal Cavity and Jet Profiles, *Phys. Rev. Lett.* **121**, 144501 (2018).
- [37] F. MacIntyre, Flow patterns in breaking bubbles, *J. Geophys. Res.* **77**, 5211 (1972).
- [38] K. E. Bigg and C. Leck, The composition of fragments of bubbles bursting at the ocean surface, *J. Geophys. Res.* **113**, D11209 (2008).
- [39] A. M. Gañán-Calvo, Revision of Bubble Bursting: Universal Scaling Laws of Top Jet Drop Size and Speed, *Phys. Rev. Lett.* **119**, 204502 (2017).
- [40] J. M. Gordillo and J. Rodríguez-Rodríguez, Comment on Revision of Bubble Bursting: Universal Scaling Laws of Top Jet Drop Size and Speed, *Phys. Rev. Lett.* **121**, 269401 (2018).
- [41] X. Wang, G. B. Deane, K. A. Moore, O. S. Ryder, M. D. Stokes, C. M. Beall, D. B. Collins, M. V. Santander, S. M. Burrows, C. M. Sultana, and K. A. Prather, The role of jet and film drops in controlling the mixing state of submicron sea spray aerosol particles, *Proc. Natl. Acad. Sci. USA* **114**, 6978 (2017).
- [42] C. R. Constante-Amores, L. Kahouadji, A. Batchvarov, S. Shin, J. Chergui, D. Juric, and O. K. Matar, Dynamics of a surfactant-laden bubble bursting through an interface, *J. Fluid Mech.* **911**, A57 (2021).
- [43] B. Ji, Z. Yang, and J. Feng, Compound jetting from bubble bursting at an air-oil-water interface, *Nat. Commun.* **12**, 6305 (2021).
- [44] X. Jiang, L. Rotily, E. Villermaux, and X. Wang, Submicron drops from flapping bursting bubbles, *Proc. Natl. Acad. Sci. USA* **119**, e2112924119 (2022).
- [45] Z. Yang, B. Ji, J. T. Ault, and J. Feng, Enhanced singular jet formation in oil-coated bubble bursting, *Nat. Phys.* **19**, 884 (2023).
- [46] F. Veron, Ocean spray, *Annu. Rev. Fluid Mech.* **47**, 507 (2015).
- [47] L. Deike, Mass transfer at the ocean-atmosphere interface: The role of wave breaking, droplets, and bubbles, *Annu. Rev. Fluid Mech.* **54**, 191 (2022).
- [48] See Supplemental Material at <http://link.aps.org/supplemental/10.1103/PhysRevFluids.8.073606> for the derivation of Eqs. (27) and (29) using the theory of the axisymmetric bubble collapse in Ref. [17] and for further details on the shape of the cavity as a function of La .

- [49] F. J. Blanco-Rodríguez and J. M. Gordillo, On the sea spray aerosol originated from bubble bursting jets, *J. Fluid Mech.* **886**, R2 (2020).
- [50] V. Lherm and R. Deguen, Velocity field and cavity dynamics in drop impact experiments, *J. Fluid Mech.* **962**, A21 (2023).
- [51] In experiments, if Oh is increased by increasing μ instead of by reducing R_b , then the condition $Bo \ll 1$ assumed here might be violated. Larger values of Bo imply different bubble shapes and different values of La below which a tiny bubble is entrapped [12,32]
- [52] A similar form of Eq. (2), deduced by us in Ref. [12], has also been recently used by Ref. [13] to calculate the initial velocity of the high speed jets after a drop impacts a liquid pool. Moreover, Eq. (2) also explains and recovers the empirical finding in Ref. [19] for $V_{jet}(T=0)$ for the case of the purely gravity driven collapse of a long bubble of height H generated from a nozzle of radius R_0 : Indeed, in this case, $\rho V^2 \sim \rho g H \rightarrow V \propto \sqrt{gH} \rightarrow Q_\infty \propto H\sqrt{gH}$ and $R_{jet}(T=0) \sim R_0$.
- [53] H. Wagner, Über stoß- und gleitvorgänge an der oberfläche von flüssigkeiten, *Z. Angew. Math. Mech.* **12**, 193 (1932).
- [54] A. A. Korobkin and V. V. Pukhnachov, Initial stage of water impact, *Annu. Rev. Fluid Mech.* **20**, 159 (1988).
- [55] S. D. Howison, J. R. Ockendon, and S. K. Wilson, Incompressible water-entry problems at small deadrise angles, *J. Fluid Mech.* **222**, 215 (1991).
- [56] G. Riboux and J. M. Gordillo, Experiments of Drops Impacting a Smooth Solid Surface: A Model of a Critical Impact Speed for Drop Splashing, *Phys. Rev. Lett.* **113**, 024507 (2014).
- [57] V. Sanjay, D. Lohse, and M. Jalaal, Bursting bubble in a viscoplastic medium, *J. Fluid Mech.* **922**, A2 (2021).
- [58] J. C. Burton, R. Waldrep, and P. Taborek, Scaling and Instabilities in Bubble Pinch-Off, *Phys. Rev. Lett.* **94**, 184502 (2005).
- [59] J. M. Gordillo, A. Sevilla, J. Rodríguez-Rodríguez, and C. Martínez-Bazán, Axisymmetric Bubble Pinch-Off at High Reynolds Numbers, *Phys. Rev. Lett.* **95**, 194501 (2005).
- [60] R. Bergmann, D. van der Meer, M. Stijnman, M. Sandtke, A. Prosperetti, and D. Lohse, Giant Bubble Pinch-Off, *Phys. Rev. Lett.* **96**, 154505 (2006).
- [61] J. M. Gordillo and M. Pérez-Saborid, Axisymmetric breakup of bubbles at high reynolds numbers, *J. Fluid Mech.* **562**, 303 (2006).
- [62] J. Eggers, M. A. Fontelos, D. Leppinen, and J. H. Snoeijer, Theory of the Collapsing Axisymmetric Cavity, *Phys. Rev. Lett.* **98**, 094502 (2007).
- [63] In Ref. [32], where the velocity field was also expressed as a line of sinks located at the axis of symmetry, we reported that, if the inertio-capillary balance held right before the instant of jet ejection, $q_\infty \propto r_{jet0}^{1/2}$. Then, from the condition for jet ejection when a bubble is entrapped for $La < 2500$, i.e., that the local Reynolds number is of order unity, namely $q_\infty \propto Oh$, it follows that $r_{jet0} \propto Oh^2$ and, from the second of the equations in (29), it follows that $v_{jet0} \propto Oh^{-1}$, recovering the results in Ref. [32]. The reason why the result of solving Eqs. (29) is similar to the one deduced assuming that the inertio-capillary scaling holds when the jet is ejected [32], can be understood in view of the results depicted in Fig. 12(b), which reveal that the exponents for $r_{jet}(\tau)$ and $v_{jet}(\tau)$ become very close to $2/3$ and $-1/3$, respectively, as $\tau \rightarrow 0$. The result depicted in Fig. 12(b) as $\tau \rightarrow 0$ can be explained in terms of the results in Refs. [12,60], where it is shown that the exponents describing the purely inertial pinch-off of bubbles become similar to the ones corresponding to an inertio-capillary collapse when the initial aspect ratio of the cavity is not large, as it is the case here.
- [64] N. C. Keim, P. Møller, W. W. Zhang, and S. R. Nagel, Breakup of Air Bubbles in Water: Memory and Breakdown of Cylindrical Symmetry, *Phys. Rev. Lett.* **97**, 144503 (2006).
- [65] A. Iafrati and A. A. Korobkin, Initial stage of flat plate impact onto liquid free surface, *Phys. Fluids* **16**, 2214 (2004).
- [66] I. R. Peters, D. van der Meer, and J. M. Gordillo, Splash wave and crown breakup after disc impact on a liquid surface, *J. Fluid Mech.* **724**, 553 (2013).